Atmospheric Dispersion of Radionuclides Following Small Modular Reactor (SMR) Accidents

by

Kimberly Catherine Mary Mitchell

A thesis

presented to the University of Waterloo

in fulfillment of the

thesis requirement for the degree of

Master of Applied Science

in

Mechanical and Mechatronics Engineering

Waterloo, Ontario, Canada, 2019

AUTHOR'S DECLARATION

I hereby declare that I am the sole author of this thesis. This is a true copy of the thesis, including any required final revisions, as accepted by my examiners.

I understand that my thesis may be made electronically available to the public.

Abstract

Small modular reactors (SMRs), reactors having a power rating of 300 Megawatts (MW) or less, have been under development for several decades. As fewer larger reactors are built due to the high upfront capital investment, interest in SMRs has increased. Some designs lack a containment structure. Designers propose that the inherent safety of SMRs justify this choice.

A projected source term for a 300 MW SMR can be devised by prorating the source term of large reactors. The source term for this study was determined by dividing the SMR power rating by that of the Fukushima reactors. The benefit of this approach is that a variety of research and measurements have been used to estimate the Fukushima source term. The source term and weather data inputs can be used to determine radionuclide dispersion following release of SMR core nuclides following an accident without any containment structure.

This study used reanalysis data, the Weather Research & Forecasting model and the HYSPLIT dispersion code to determine meteorological fields and analyze public dose rate and total dose. The analysis performed determined that a release, similar in composition to that of a Light Water Reactor, would result in unacceptably high public doses unless a containment system were in place.

Acknowledgements

I would like to acknowledge the support of my supervisors, Dr. Fue-Sang Lien of the Mechanical and Mechatronics Engineering Department and Dr. Michael Waite of the Applied Mathematics Department. Their input and encouragement helped me refine my ideas and organize my thoughts into the work documented in this thesis.

I also acknowledge the support of my occupational health nurse, Karen Johns, and my occupational therapist, Roxanne Andrews. Upon finding myself with post-concussion syndrome at the half-way point of my program I was not sure I would finish. Karen and Roxanne helped me learn the 'new' me and convinced me that I could contribute.

Finally, I acknowledge the support of the Qalipu Mi'kmaq First Nation. Their financial support made it possible to secure the supervisors I count myself fortunate to have had.

Dedication

To my mother. I am grateful to have inherited her fortitude and capacity to dream.

To my children. I am humbled to have had the opportunity to show you that you can achieve whatever your mind conceives.

To my partner. I am blessed to have your love and support.

Table of Contents

List of Figures

List of Tables

Chapter 1

Introduction

Small modular reactors (SMRs) include those reactors with rated power less than 300 megawatts thermal (MWt) (International Atomic Energy Agency [IAEA], 2019). Work has been progressing on small modular reactor design and construction for several decades. This work, however, remained on the fringe since reactor development and construction focused on large reactors throughout the 1970s and 80s. Following the accidents at Three Mile Island in 1977 and Chernobyl in 1986, the potential risk of nuclear accidents became publicly apparent (Blix, 1986). Both of the reactor accidents involved uncontrolled reactors that underwent large power increases.

In the case of Three Mile Island, located in Pennsylvania, United States, the reactor fuel partially melted. Containment features of that reactor prevented radioactive releases having any impact to plant personnel or the public (Nuclear Regulatory Commission, 2018). At Chernobyl, located in Ukraine, control rods were removed during a reactor test that led to a massive, uncontrolled reactor power increase. Fuel melted and reactor components caught on fire. An explosion occurred and lifted the reactor cover off its structure. The reactor did not feature a containment structure. This accident would result in large releases of radioactivity that spread in Belarus, Russia, Ukraine, and across Europe (United Nations Scientific Committee on the Effects of Atomic Radiation, 2012).

Construction of new large plants was drastically slowed. Some projects that were not yet started were cancelled. The focus of the nuclear power industry turned to high performance

operation of in-service plants. The Institute for Nuclear Power Operations (INPO) and the World Association of Nuclear Operators (WANO) formed to establish and hold member plant operators to high standards with a goal of continual improvement in plant operation (Cantelon, 2016).

Over the next two decades operations improved steadily. In 2011 the Fukushima Nuclear Power Plant experienced a multi-unit reactor accident following an earthquake which triggered a tsunami. The aftermath of the accident was broadcast around the world through social media, the internet, and traditional media. Public support for large conventional nuclear power dropped. Some countries, most notably Germany, vowed to end their use of nuclear power as an energy source. In Japan, home of the Fukushima Dai-ichi plant, all reactors were shut down pending safety reviews (World Nuclear Association, 2018). Overall, the conventional nuclear power generation industry (i.e. use of large reactors) has not yet recovered from the negative impact of the Fukushima accident.

These circumstances presented an immense opportunity for the small modular reactor concept. They are inherently passively safe and adaptable to multiple sites without the need for expensive transmission infrastructure (International Atomic Energy Agency, 2019). In order to construct and operate an SMR, a proponent would need to obtain the required licences from the Canadian Nuclear Safety Commission (CNSC). A key input into the license review process is a safety analysis of the SMR. This includes an analysis of the radionuclide dispersion amount and location should a worst-case accident occur.

This thesis reviews the current literature related to atmospheric dispersion of radionuclides following reactor accidents. Research modelling methods and assumptions are

examined for a notional small modular reactor assumed to be constructed at the Chalk River, Ontario, Canada nuclear facility. Meteorological simulation results are compared to measured data and radiological deposition is calculated. Finally, conclusions are drawn regarding the adequacy of small modular reactor enclosure structures.

Chapter 2
Literature Review

2.1 Dispersion Modelling Overview

There are two approaches to determining how a pollutant moves through the atmosphere. Each involves using the mass, momentum, energy transfer, and pollutant concentration equations together. These equations are covered in more detail in Chapter 3. The two approaches are known as the Eulerian approach and the Lagrangian approach. When the Eulerian approach is used, fluid is viewed as a continuum. This is useful since the differential form of the mass, momentum, and energy transfer equations can be solved on a fixed grid. A downside to this approach is that the computational power needed to use these equations to determine dispersion by coupling mass, momentum, and energy equations is prohibitive.

The approach that tends to be used for dispersion modelling employs the Lagrangian form of the equation for pollutant concentration. The strength of the Lagrangian approach is that non-linear fluid advection terms do not need to be determined explicitly. Conceptually, approximations made in order to solve the Lagrangian equation involve only velocity. Use of Lagrangian equations eliminate partial derivates. However, this approach can quickly become computationally expensive when large numbers of fluid particles are tracked (Vié et al, 2014). The Lagrangian equations are coupled in a manner that, rather than treating a pollutant as a continuum, treats it as a series of particles. This approach has grown into the field known as 'atmospheric dispersion modelling' or ADM. This approach begins with a meteorological field comprised of wind, temperature, precipitation, and pressure.

For this study, the Eulerian equations of the Weather Research & Forecasting (WRF) model were used to determine the meteorological field. The field was calculated using a numerical approximation of the momentum, continuity, and energy equations. Once the field was established, pollutant concentration was determined using the Lagrangian form of the mass equations along with the momentum and energy transfer equations as implemented in the HYSPLIT analysis code and described by Draxler and Hess (2018).

In practice, pollutant dispersion is calculated by breaking down particle movement into modes of transport. Wet transport depends on the particle settling velocity, pollutant solubility, and amount and type of precipitation while dry transport depends on particle settling velocity only (Sportisse 2007). Various simplifications may be made that eliminate one or more of these dependencies. One such simplification is the assumption that wet transport due to particle settling is negligible when compared to dispersion due to dissolution or precipitation. An example of numerical simplification involves modelling particle transport by defining a scavenging coefficient, Λ, that reduces the mass transport equation to a first-order ordinary differential equation. Examples of such coefficients are given below in Table 1 (Sportisse, 2007).

Atmospheric dispersion modelling was first used to predict the spread of radioactivity after reactor accidents following the Chernobyl reactor accident in 1986. The Chernobyl reactor was a Soviet design that produced 1000 Megawatts (electrical). The reactor design featured a core that was 7 meters high and 12 meters in diameter. There was a reactor building surrounding the core, but no structural containment enclosure (World Nuclear Association, 2018). State-of-the-art atmospheric dispersion model resolution at this time was coarse but did provide a tool to

predict the spread of radioactivity. In the United Kingdom, Imperial College used a Lagrangian puff model while the United States Atmospheric Release Advisory Center used Gaussian puffs within an Eulerian domain to do prediction calculations (Benamrane et al, 2013). The models were not generated quickly enough to use for emergency planning purposes. In the two decades following, advances in science and technology would improve model resolution and accuracy (Benamrane et al, 2013).

In 2011, a multi-unit accident at the Fukushima Dai-ichi nuclear power plant occured following a tsunami. The accident provided a unique opportunity to further refine atmospheric dispersion models for use following nuclear accidents. Data sets including weather parameters and radiation dose measurements have been made available to researchers and modellers by the Japanese agency response for nuclear power regulation and the Tokyo Electric Power Company (TEPCO) – the company responsible for the plant's operation. The data has largely been used to validate the ability of different models to predict the direction and amount of radioactive particle deposition (Benamrane et al, 2013).

Sportisse (2007) summarized various parameterizations used in radioactive dispersion models. He grouped the sources of uncertainty into two categories: meteorological field uncertainty and microphysical uncertainty. Sportisse focused on a method to define the wet scavenging uncertainty and developed a piece-wise function to describe wet radioactive deposition. In order to develop the deposition function, the uncertainty was broken down into two sources: unknown aerosol distribution and unknown rainfall intensity. Sportisse began by stating that wet deposition processes are parameterized by,

$$\frac{dc}{dt} = -\Lambda c, \tag{1}$$

where c is concentration and Λ is the scavenging coefficient, per second (Sportisse 2007). Because particles will have a size distribution, the number of particles – n_p in the equation given by Sportisse – was assumed to be suitably represented using the following differential equation,

$$\frac{dn_p(d_p)}{dt} = -\Lambda(d_p)n_p(d_p), \tag{2}$$

where d_p is particle diameter in micrometers, $dn_p(d_t)/dt$ is the scavenging rate, and Λ is the scavenging coefficient, per second (Sportisse, 2007).

Sportisse used data from radar measurements after the Chernobyl accident to construct an empirical model for the scavenging coefficient,

$$\Lambda \cong [10^{-5} - 10^{-3}]p_0^{[0.5-0.7]}, \tag{3}$$

where p_o is rainfall intensity (millimeters per hour) (Sportisse 2007). In order to determine rainfall intensity a scavenging coefficient is assumed based on a range of aerosol particle sizes, where r_p is particle radius in micrometers. A sample of Λ values is given in Table 1.

Species Type	Scavenging coefficient, Λ (per second)
Reactive iodine	$\cong 10^{-4}$
Organic iodine	$\cong 10^{-6}$
Submicronic particles $r_p < 1$ μm	$\cong 5 \times 10^{-5}$
Particles $r_p = 5$ μm	$\cong 10^{-4}$
Coarse particles $r_p = 10$ μm	$\cong 5 \times 10^{-4}$

Table 1 - Scavenging coefficients used by Sportisse (2007)

Korsakissok et al (2013) used the Fukushima data to perform a dispersion concentration sensitivity analysis. Their objective was to identify the most sensitive simulation parameters and input data. The sensitivity analysis employed a Gaussian puff model developed by the Institut de radioprotection et de sûreté nucléaire (IRSN) called pX (Didier et al, 2015). The baseline simulation utilized a spatial grid of 0.125 degrees by 0.125 degrees and a 3-hour time step. The radioactive source term included seventy-three isotopes and was based on a notional Pressurized Light Water reactor of the type operated in France. This study found that modelled wind speed was higher than measurements by approximately 50%. It found that calculated wind direction agreed with observations two-thirds of the time. Because of the importance of wind direction on atmospheric dispersion model results the authors chose to augment the modelled weather field with observed data on those occasions when the model calculated an incorrect wind direction. This was done by substituting the measured value for the calculated value in the results. Particle

deposition velocity was taken to be 0.2 centimeters per second from Brandt et al (2002). The authors assumed that two-thirds of released Iodine was in gaseous form with one-third being particulate. The molecular Iodine deposition velocity was taken to be 0.7 centimeters per second from Baklanov & Sorenson (2001). The authors used the wet scavenging model developed by Terada et al $\Lambda_s = \Lambda_o P_o^B$ where Λ_o is the scavenging constant, 5 x10^{-5} h/mm.s, B is a pro-rating factor, 1, and P_o is rainfall intensity in millimeters per hour (Korsakissok et al, 2013). Terada set B to 0.8. Neither Terada nor Korsakissok give a rationale for selection of this value.

Dose coefficients, as determined by Eckerman and Ryman (1993), were used to calculate dose rate.

The results of the sensitivity study determined that the analysis was most sensitive to assumptions regarding gas and aerosol partitioning, proportion of organic versus inorganic Iodine, and aerosol size distribution. The most important input data included reactor source term, standard deviation, and wind direction. While the model had limitations, such as weather field accuracy, atmospheric dispersion modelling is still useful since it fills in data gaps due to the discrete nature of gamma detection devices and soil and air sample analyzers.

Another sensitivity study was carried out by Hu et al (2014). The focus of this study was somewhat different than Korsakissok et al in that they concentrated on the microphysical and diffusion schemes that most strongly influenced radioactivity deposition. Another difference is that Korsakissok utilized the pX model coupled with a Gaussian puff model, while Hu et al chose to use the Weather Research and Forecasting (WRF) model (Skamarock et al, 2008) coupled with WRF-Chem. The reason for this approach was to eliminate human and rounding errors due

to data transfer between the weather model and dispersion model. The first objective of this study was to determine the most parameters having the greatest influence on deposition. Secondly, the relative importance of wet and dry deposition was examined. The authors compared results using a 1.5 order Turbulent Kinetic Energy (TKE) scheme and a horizontal Smagorinsky scheme to predict mixing and deposition. Based on results generated by the two analyses, they determined that the TKE scheme performed better. Regardless of the scheme used, the model did not perform well for mountainous terrain. Assumptions regarding the source term were found to have a strong impact on the deposition rate. Unfortunately, this study did not lead to any specific conclusions regarding the importance of wet and dry deposition in spite of error analyses using percentage bias, percentage root mean square error, and mean bias error methodologies. This study did conclude that assumptions regarding reactor accident source term can impact calculated deposition by approximately five times. An open question, however, is whether this is significant given the large releases of radioactivity following conventional light water reactor accidents. A related question is whether source term assumptions have a meaningful impact on environmental deposition following Small Modular Reactor accidents.

Given the sensitivity to assumptions regarding the source term, as established by Hu et al, a number of studies have attempted to validate source terms assumed for Fukushima Dai-ichi reactors. This paper assumed that Cesium-134 was released in equal amounts and at the same rate as Cesium-137. The Cesium-134 source term has been previously validated by Terada et al (2012). Unlike the other two studies reviewed, this study used a Lagrangian model known as WSPEEDI-II to calculate deposition and dose. Unfortunately, no definitive conclusions could be drawn using the study results.

Achim et al (2014) authored a study that used WRF and FLEXPART codes. The FLEXPART code is a Lagrangian code used to analyze atmospheric dispersion. Weather data for this study was sourced from the National Centers for Environmental Prediction Global Forecast System. The source term used in this study was assumed to include 6×10^{18} Becquerels of Xenon-133, 1×10^{16} Becquerels of Cesium-137, and 1×10^{17} Becquerels of Iodine-131. The simulations in this study could not reproduce the measured results for radioactive deposition following the Fukushima nuclear accident.

Srinivas et al (2012) also utilized the WRF, HYSPLIT, and FLEXPART codes. Rather than attempt to validate a source term, this research group aimed to determine the validity of the code results. The source term provided by the Japanese government was used directly. These estimates include 1.2×10^{16} Becquerels of Cesium-137 and 1.5×10^{17} Becquerels of Iodine-131. While this approach greatly simplified the dispersion modelling since the complete composition and time-based change in release rates was not considered, it did introduce a significant point of weakness – dose rates from isotopes other than Cesium-137 were unknown and so were excluded from the data. This is impactful since Iodine-131 dose and Xenon-133 dose tends to substantially increase effective whole-body dose. It would be reasonable to assume the effective increase would at least double whole-body dose since Iodine-131 is released in quantities approximately equal to Cesium-137 and is taken in by humans at least as easily, arguably more so due to the thyroid's propensity for iodine absorption.

The WRF Advanced Research and Weather (ARW) core was used by Srinivas et al (2012) to generate the meteorological fields while FLEXPART provided atmospheric dispersion calculations. HYSPLIT was used to compute advection of a single radioactive particle and its

trajectory. While WRF does have a dedicated module for this purpose, WRF-Chem, the benefit of using FLEXPART is that radioactive species decay is already included in FLEXPART. If WRF-Chem is used then the code must be modified to incorporate radioactive behaviour – including decay, decomposition, chemical reactions, and atomic reactions. Additionally, FLEXPART can use WRF output data directly without manual code modifications. HYSPLIT also includes radioactive species decay and can use WRF output data directly.

The analysis performed by Srinivas et al (2012) attempted to replicate atmospheric conditions to the extent allowed by the state-of-the-art. Using a model domain of 3375 kilometers square with a horizontal resolution of 15 kilometers and a nested domain of 1325 kilometers by 1220 kilometers with a horizontal resolution of 5 kilometers, the WRF calculations considered both wet and dry deposition. Wet deposition was modelled using an exponential decay process that considered moisture effects of clouds and rain. Dry deposition was modelled using deposition velocity with the resistance deposition model. The dry deposition model was similar to the approach taken by Korsakissok et al (2013).

In the Srinivas study, radioactive dose pathways considered included gamma radiation 'shine' from overhead radioactive clouds, inhaled particulates and vapours, and ground deposited radioactive material. In order to establish an exposure period, the researchers considered the time period over which the Fukushima Dai-ichi reactor accident occurred. It was established that radioactive releases occurred from March 11th to 23rd and decreased exponentially afterward. The geographical topography of the region surrounding Fukushima includes a combination of flat, inland regions, mountainous terrain, and coastal regions. As in other studies, the model performance was best for flat, inland terrain. Srinivas et al (2012) compared measured data with

simulation results for wind speed, wind direction, temperature, and relative humidity. Rainfall was poorly simulated although there was good agreement between the model and measurements for one day of the thirteen considered in the study. The model did not perform well in terms of predicting rain location for days with low and moderate rainfall amounts. FLEXPART model performance was somewhat better since the analyzed dispersion pattern represented the measured pattern fairly well. This gives rise to the question of whether the meteorological field really has that much of an effect on radiation dose to the public. It was expected that rainfall would be a key driver in determining dose. The delta between the expected and actual result is not explained, providing an opportunity to further validate these results.

Unlike other studies that hesitated to draw any conclusions, Srinivas et al (2012) did suggest that model difficulties could be due to insufficient grid resolution. Their study also concluded that wet deposition dominated over dry in the case of Fukushima. This is not particularly surprising since fine particulates tend to settle slowly under the force of gravity only. One question worthy of further examination is whether water – either in vapour, liquid, or solid form – is the most important factor in determining the extent and amount of atmospheric dispersion of radiation following reactor accidents. The data required to analyze reactor accidents in this context will hopefully never be available owing to the fact that such a small number of accidents occur that the statistical significance of a single result is negligible. In the event that moisture is an overwhelmingly important factor in predicting atmospheric radionuclide dispersion, the impact will attempt to be controlled in the current analysis by carefully considering the atmospheric moisture budget when selecting the simulation start date and end date.

Generally, the Fukushima work was exceptionally informative in terms of identifying the relative importance of meteorological and dispersion parameters. In spite of substantial social and economic impacts, the long-term outcome at Fukushima is quite positive. For example, the United Nations Scientific Committee on the Effects of Atomic Radiation (2015) found lower rates of thyroid cancers and adverse pregnancy outcomes in the area adjacent to Fukushima compared to other prefectures of Japan – termed 'non-exposed' – and utilized as a control group.

For small reactors, the anticipated radiation dose has been studied for several different reactor types. One study looked at a one Megawatt (thermal) research reactor. Another analyzed radiation dose for a small modular High Temperature Gas-cooled Reactor (HTGR).

In the case of the research reactor, radiation dispersion was analyzed by Zeggar et al (2017) using a Gaussian plume model following destruction of all fuel elements after an airplane crash. Although it is highly unlikely that all fuel elements would be destroyed in even a worst-case event, this scenario provides a bounding case. The analysis concluded that total radiation dose remains within the reference level range established by the International Atomic Energy Agency in the IAEA Safety Standard for protection of the public and the environment (IAEA, 2018). An interesting point to note regarding the outcome of this study is that the calculated radiation dose for wet versus dry deposition differed by less than 5%.

The small modular HTGR was analyzed by Ding et al (2018). In their study, the researchers performed an analysis similar to the deterministic safety analysis that is required to be performed by operators of conventional nuclear reactors. For this study, the authors chose to analyze an event known as a Large Break Loss of Coolant Accident (LBLOCA). This event

occurs when the main reactor coolant circuit of the nuclear power plant undergoes a guillotine break in the piping. Mitigation of this event in large pressurized water reactors typically requires adequate functioning of a containment structure in order to protect the public and the environment from a large release of radioactivity. This study used a Gaussian plume module and calculated an effective dose based on distance from the reactor. The calculated dose 200 meters from the reactor on the day of the accident was 200 milliSieverts. This radiation dose is the same dose that would be received if a person underwent approximately ten Computed Tomography (CT) scans of the abdomen and pelvis with and without contrast (Mahesh, 2018). By day 2 and day 7, the analysis projected an effective dose of 20 milliSieverts – or one CT scan.

The effective dose results from this study would also fall within the IAEA recommended limits assuming the reactor featured an exclusion zone, within which no members of the public would reside. In order to be within the IAEA recommended limits, the particular reactor design analyzed incorporated design features such as a negative temperature feedback, inherently safe fuel design, and passive heat removal to ensure elimination of accidents that result in severe core damage and large radioactivity releases.

A third outcome of the Fukushima reactor accident is that the safety of Small Modular Reactor designs is being re-examined using lessons learned in the past following severe accidents. The role of the containment structure and the use of probabilistic safety analysis has been studied in the context of Small Modular Reactor design and operation. An example of this is documented in the IAEA technical paper outlining design lessons-learned for SMRs as a result of the Fukushima nuclear accident (2016).

Chapter 3
Theoretical Basis

The evolution of radionuclide dispersion in the atmosphere following a SMR accident is governed by atmospheric fluid dynamics and mass transport processes. The equations of energy, momentum, and mass transfer can be used to determine the atmospheric velocity field, which governs radionuclide deposition location and rate. In order to solve these equations boundary and initial conditions are required.

The continuity equation is

$$\frac{\partial \rho}{\partial t} = -\nabla \cdot (\rho \boldsymbol{v}), \tag{4}$$

where ρ is the fluid density and **v** is the fluid velocity vector.

The energy transfer equation is

$$\rho \hat{C}_p \frac{DT}{Dt} = k\nabla^2 T - (\nabla \cdot \boldsymbol{q}), \tag{5}$$

where **q** is the heat flux vector, $\hat{C}_p$ is specific heat at constant pressure, T is temperature, t is time, k is thermal conductivity (Price, 2006). The term $\frac{DT}{Dt}$ is the substantial derivative of temperature. The substantial derivative term – in expanded form – is,

$$\frac{DT}{Dt} = \frac{\partial T}{\partial t} + v_x \frac{\partial T}{\partial x} + v_y \frac{\partial T}{\partial y} + v_z \frac{\partial T}{\partial z}, \tag{6}$$

where v_x, v_y, and v_z are components of the velocity vector (Bird, Stewart & Lightfoot 2007). The substantial derivative represents the change in temperature with time following the position of a particle in motion.

The momentum transfer equation is

$$\frac{D\boldsymbol{v}}{Dt} = -\nabla p + \rho \boldsymbol{g} + \mu \nabla^2 \boldsymbol{v}, \tag{7}$$

where **v** is the particle velocity, p is pressure, μ is viscosity, ρ is density, **g** is the force due to gravity, and t is time (Juniper, 2015, Bird, Stewart, and Lightfoot, 2007 & Price, 2006).

The pollutant mass transfer equation is

$$\frac{dc_i}{dt} = \kappa \nabla^2 c_i - D_i, \tag{8}$$

where c_i is concentration of species i, D_i is a decay term for species i that includes species changes due to molecular and radioactive decay, and κ is molecular diffusivity (Wilson & Sawford, 1995). This equation neglects any generation, destruction, and chemical reactions occurring within the fluid parcel.

3.1 Numerical Solution Using WRF

Energy transfer in the atmosphere is most commonly experienced as a temperature difference which results in buoyancy forces and fluid motion. Heat may be transported in the atmosphere through a combination of heat diffusion, turbulent mixing, and buoyant mixing. The code used in this study to simulate the meteorological field is the Weather Research & Forecasting (WRF) model (Skamarock et al, 2008). The WRF model was chosen as it was developed to be a flexible operational forecasting model with a larger user base across the globe. It is efficient to run and readily available for use on the graham High Performance Computing (HPC) cluster maintained by Compute Canada.

The momentum, mass, and energy transfer equations must be solved using numerical techniques in the case of the three-dimensional time-varying flows found in the atmosphere. A key step in WRF achieving computational efficiency was the re-statement of these equations with hydrostatic pressure as the independent variable. This coordinate transformation is accomplished by defining η and μ as follows,

$$\eta = \frac{(p_h - p_{ht})}{\mu}, \mu = p_{hs} - p_{ht}, \tag{9}$$

where η is the vertical coordinate, μ is the hydrostatic pressure difference from the surface of the earth to the top of the domain, p_h is the hydrostatic pressure at the vertical layer, p_{hs} is the hydrostatic pressure at the earth's surface, and p_{ht} is the hydrostatic pressure at the top boundary of the domain (Skamarock et al, 2008).

Realistic simulations are achieved in WRF by incorporating moisture, the Coriolis force, a variety of physics parameterizations, and incorporating measures to account for boundary effects due to the earth's curvature. This approach allows the user to utilize the physics most appropriate for the problem being solved without having to modify the ARW solver source code. One objective of this study is to determine the relative effect of moisture on radionuclide deposition. Moisture effects in WRF ARW are calculated using mixing ratios, or mass of water per mass of dry air, to determine the contribution of each form of atmospheric moisture to the overall air density. In other words,

$$\alpha = \frac{\alpha_d}{1 + q_v + q_c + q_r + q_i + \cdots}, \tag{10}$$

where α is the inverse density of moist air, α_d is the inverse density of dry air, q_v is the mixing ratio for water vapour, q_c is the mixing ratio for clouds, q_r is the mixing ratio for rain, and q_i is the mixing ratio for ice (Skamarock et al, 2008).

The variables for geopotential ϕ=gz, pressure p, and dry air mass μ_d are split into two parts – one hydrostatic and one perturbation. This gives

$$p = \bar{p}(\bar{z}) + p', \phi = \bar{\phi}(\bar{z}) + \phi',\ \mu_d = \overline{\mu_d}(x, y) + \mu_d', \tag{11}$$

where geopotential and pressure are functions of height only while dry air mass is a function of position.

3.2 Radionuclide Mass Transfer

In this study, mass transfer analysis is focused on the movement of radiological species in the atmosphere from a point source. Three species of interest, due to their effect on human health and the environment, are Iodine-131 (I-131), Xenon-133 (Xe-133), and Cesium-137 (Cs-137). I-131 is of interest since it is readily taken up by humans and the environment. In the human body, I-131 concentrates in the thyroid gland leading to tissue damage. Xe-133, as a noble gas, does not react in the human body or the environment. It is of interest since it is often released in large amounts early in the nuclear accident event sequence. Cs-137 is released in particulate and aqueous pathways following nuclear reactor accidents. It is of interest largely due to the high volume of release during nuclear accidents, its long half-life of 30 years, and its highly reactive nature.

Three different codes were evaluated for use in determining radionuclide dispersion path and amount: WRF-Chem, FLEXPART-WRF, and HYSPLIT.

WRF-Chem, as an integrated WRF component code, is specifically designed to receive the meteorological field calculated by WRF. This reduces post-processing effort and the potential for errors induced by incorrectly transferring WRF output data to a different code. Unfortunately, WRF-Chem does not contain any of the calculations or parameters necessary to determine radioactive decay or dose. WRF-Chem is targeted toward the environmental community and, as such, the source code would require a number of modifications prior to use. The need for modifications provides another potential source of error.

FLEXPART-WRF contains the calculations and parameters necessary to determine radioactive decay and dose. Because it is not a component code of WRF, its use requires post-processing effort. This post-processing effort was greatly reduced when a version of FLEXPART was released that was designed specifically to work with WRF output files (Brioude et al, 2013). In addition to consuming NetCDF format input files, FLEXPART-WRF could generate output files in NetCDF format. This would allow the WRF user community to easily utilize existing WRF utility programs able to work with NetCDF files. The ability to work directly with WRF output files and the existing ability to analyze radiological processes make FLEXPART-WRF a high potential code. A drawback of FLEXPART-WRF is that detailed user documentation and support are not readily available.

Like FLEXPART-WRF, HYSPLIT is capable of calculating radioactive decay and deposition. Unlike FLEXPART-WRF, HYSPLIT cannot process NetCDF files directly.

However, HYSPLIT is supplied with a conversion utility for converting NetCDF files into a file type that can be consumed by HYSPLIT. In addition, HYSPLIT is capable of processing binary files – which is a file format WRF can generate by changing the output format in the namelist.input file used to run WRF. Because HYSPLIT is supported by the National Oceanic and Atmospheric Administration (NOAA), the user community and code documentation were readily accessible. Since this code has the same ability to analyze radioactive dose, it was selected as an alternative to FLEXPART-WRF.

HYSPLIT is a Lagrangian dispersion code. In order to numerically determine dispersion trajectories and concentrations, HYSPLIT uses pre-processed meteorological input data. This data can be downloaded from the HYSPLIT data archive or generated using WRF or another meteorological code. While Lagrangian analysis codes often use either a particle dispersion or a puff approach to calculation species concentration, HYSPLIT uses a hybrid approach. Vertically, the concentration field is determined using a particle approach while horizontally, the puff approach is used. In a puff model, the species under consideration is split into a number of puffs or clouds. The position of each puff is then calculated as if it were a particle while the concentration of the species inside the puff is assumed to have a Gaussian distribution (Draxler & Hess 2018).

In order to determine the turbulent velocity component, HYSPLIT calculates turbulent velocity in the atmosphere – both in and above the boundary layer. This calculation involves determination of:

- the Obukhov length from friction velocity and temperature,

- pollutant vertical mixing from surface fluxes within the atmospheric boundary layer and vertical diffusivity above the boundary layer, and
- horizontal mixing from velocity deformation as described by Smagorinsky (1963) and Deardorff (1973).

The turbulent velocity is then used to calculate the puff and particle positions as a function of time. The equations are discussed in more detail in Section 4.3.1..

In addition to dispersion, HYSPLIT also has the ability to calculate three modes of deposition: dry, wet, and radioactive decay. This is useful for analyzing radioactive releases since environmental dose rates can vary depending on the dominant deposition mechanism at the time the release(s) occur. This model, like others, uses particle size and density to determine particle settling velocity. Wet deposition calculations use Henry's Law constant to determine deposition rates for soluble gases and scavenging ratio for particles. Radioactive decay is determined on a mass-basis using the half-life of the species under consideration. In this case, the mass is given by:

$$m(t + \Delta t) = m(t) \cdot e^{-\beta_{rad}\Delta t}, \tag{12}$$

where m is the mass of material undergoing radioactive decay, β_{rad} is the radioactive decay constant, ln 2 / $T_{1/2,}$ $T_{1/2}$ is the species half-life (Draxler & Hess, 2018).

3.3 Research Scenario

The simulation performed is for a worst-case SMR accident with no containment mitigation. It is important to understand the dispersion following such an accident because this

information forms the basis for SMR containment requirements, siting requirements, and emergency planning. It is important to note that a key assumption of this study is the composition of the SMR core inventory released into the atmosphere. This is the parameter referred to as 'source term'. Substantial effort has been put into establishing a practical source term.

Caution must be taken when applying the results of this study in order to draw conclusions regarding a particular SMR technology. The novelty of SMR core designs means that the results of this study may not apply to all SMRs.

3.4 Source Term

In this study, 'source term' refers to the isotopic make-up of the material released from the reactor. Specifically, the source term denotes the radioactive material available to be released into the environment following a worst-case accident. A number of studies have attempted to estimate the source term for the Fukushima nuclear accident. Korsakissok et al (2013) used a source term consisting of 73 different radionuclides. This spectrum is based on conventional light water nuclear reactor core inventory adjusted for the smaller core found in an SMR. Table 2 shows the radionuclide quantities for the main species that have been prorated to reflect the smaller SMR reactor size.

Isotope	Quantity (Bequerels)
Iodine-131	1.97×10^{17}
Iodine-132	1.68×10^{17}
Tellurium-132	1.08×10^{17}
Cesium-137	2.06×10^{16}
Cesium-134	2.78×10^{16}
Xenon-133	5.94×10^{18}

Table 2 - Reactor core inventory; Korsakissok et al (2013)

This approach is in contrast to the approach taken by Morino et al (2011) that quantified the source term using Iodine-131 and Xenon-133 only. Morino et al (2011) utilized a source term of 1.42×10^{17} Bq and 9.94×10^{15} Bq for I-131 and Xe-133, respectively. Chino et al (2011) took a similar approach to Morino and obtained a similar, although not exact, result. Chino et al (2011) determined a source term for I-131 and Xe-133 of 1.5×10^{17} Bq and 1.3×10^{16}, respectively. Stohl et al (2012) used yet another unique approach by using a FLEXPART inversion algorithm to generate a source term prediction using a 'first guess' emission amount. The Xe-133 quantity was determined to be 1.53×10^{19} Becquerels $\pm$ 0.31×10^{19} Becquerels. The Cs-137 quantity was determined to be $3.66 \times 10^{16} \pm 1.65 \times 10^{16}$ Becquerels. It is notable that the study by Stohl et al (2012) excluded any dose from I-131. Although I-131 has a short half-life of approximately 8 days, its impact on human health cannot be discounted since it is so readily absorbed by the human body.

It is important to note that Srinivas et al's (2012) simulations were for radionuclide releases from up to six Light Water Reactors (LWRs) with an approximate total capacity of 6 000 Megawatts. By definition, an SMR has a capacity of 300 Megawatts or less. For this study, a prorated source term has been used that is just 5% of the Fukushima source term (i.e. 300 MW/6000 MW).

In order to establish a quantity for Iodine-131 particulate and gas fraction, the work of Korsakissok et al (2013) and that of Achim et al (2014) were taken in combination. Korsakissok et al (2013) determined a total Iodine-131 amount to be 1.97×10^{17} Bq while Achim et al (2014) reported an Iodine-131 gas fraction for Fukushima accident of 71% plus/minus 11%. This was rounded to 70% for the current study. Cesium-137 and Xenon-133 quantities were established using the results of the work by Stohl et al (1998). As described above, Stohl et al (2012) established a range for the Cesium and Xenon releases from Fukushima. This method incorporates the uncertainty that surrounds release amounts following the series of reactor accidents. The upper bound of the release range was prorated to adjust for the single, smaller reactor core of an SMR. The source term used for this study is summarized in Table 3.

Isotope	Quantity (Becquerels)
Iodine-131 particulate	0.591×10^{17} Ref. Korsakissok et al Ref. Achim et al; gas/particulate ref
Iodine-131 gas	1.379×10^{17} Ref. Korsakissok et al Ref. Achim et al; gas/particulate ref
Iodine-132	Excluded from release
Cesium-134	Excluded from release
Cesium-137	2.66×10^{15} Ref. Stohl et al; upper bound Ref. Chino et al; ratio assumption
Xenon-133	9.20×10^{17} Ref. Stohl et al; upper bound

Table 3 - Radioisotopes and quantities used in this study

Iodine-132 has a half-life of 2.295 hours and is generated when Tellurium-132 decays releasing a beta particle (Gray et al, 2017). Because of its short half-life Iodine-132 was not included in the source term used in this study.

Cesium-134 has a half-life of 2.0652 years. Cesium-134 decays to either Xenon-134 or to Barium-134. The probability of decay to Xenon-134 is 0.0003% and is, therefore, assumed to not occur. Decay to Barium-134, a stable isotope, occurs upon release of a beta particle. Cesium-137 also has decays by releasing a beta particle. It, however, has a much longer half-life of 30.08 years (Gray et al, 2017). Because beta radiation is relatively low energy it must generally be inhaled, ingested, or injected in order to have any biological effect. Once in the body, long term exposure is typically needed to have any consequential effect. As a result, Cesium-134 releases were excluded from releases used in this study.

The source term release was made over a 24-hour period for this study. It was assumed that a single release occurred. This is a reasonable assumption for a single reactor unit. Modular

reactors that are to be built as multi-unit sites should be analyzed for multiple releases occurring within a 24-hour period.

Chapter 4
Simulation Set-up

4.1 Geographical Region

The WRF and HYSPLIT analysis is completed for a hypothetical small modular reactor located near the town of Deep River, Ontario, Canada. This geographical region was chosen because of the historical placement of Atomic Energy of Canada Limited's Chalk River facility. This facility has been the site of some of Canada's greatest contributions to our understanding of nuclear science and engineering. This is a logical choice for a reactor site.

An overview of the specific location can be found in Figure 1 and a more granular map is given in Figure 2.

Figure 1 - Overview of Small Modular Reactor site topography (Government of Canada, 2018). Approximate WRF simulation domain enclosed by blue lines

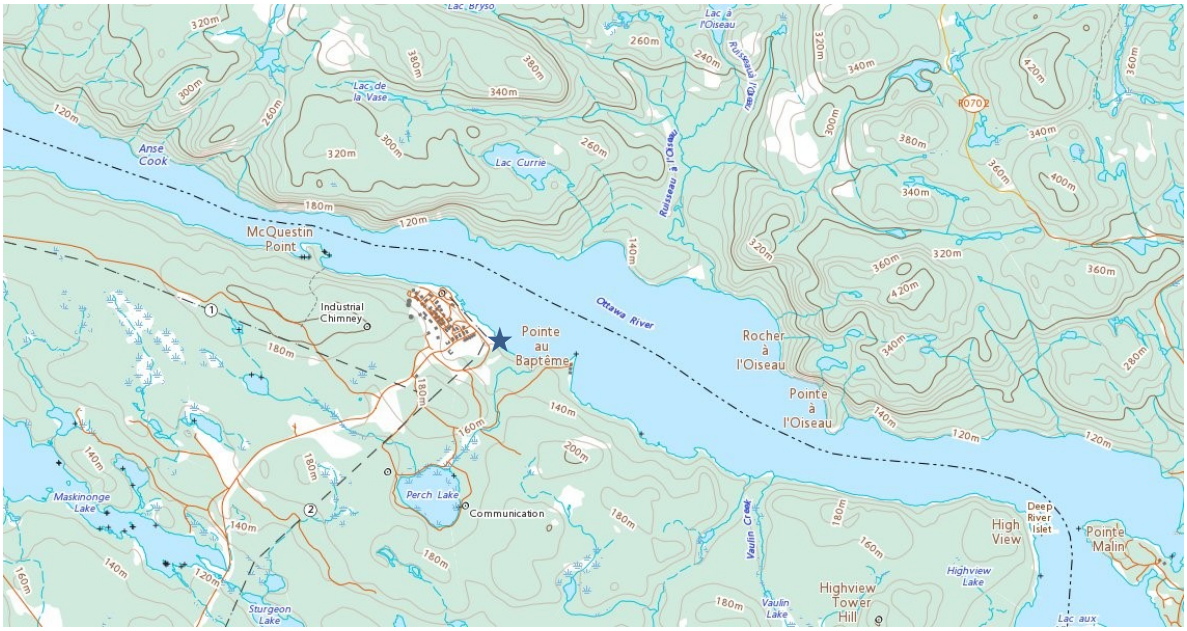

Figure 2 - 1:50 000 view of hypothetical SMR site (Government of Canada, 2018).

The postulated reactor site is located at Geographical Positioning System (GPS) coordinates of 46.049° North latitude, 77.358°West longitude. This location is approximately 1 kilometer west north-west of Pointe au Baptême and is adjacent to the Ottawa River. The approximate location is denoted by a star in Figures 1, 2 and 3. The SMR would be located next to the river to provide a source of service water.

Dispersion analysis was completed using two different meteorological datasets – a reanalysis dataset and a generated dataset. The reanalysis dataset had a grid size of 1-degree latitude by 1-degree longitude. The generated dataset was created using WRF. In the WRF simulation, a geographical data resolution of 0.9 kilometers was used with a model grid size of 1 km by 1 km. It was anticipated that there may be some simulation issues due to the large reduction from the input data grid of ~110 kilometers to the WRF grid size of ~1 kilometer. To reduce any possible impact, the domain was increased to span an additional 48 kilometers in the

vertical direction and an additional 22 kilometers in the horizontal direction. The east-west simulation domain spanned 148 kilometers and the north-south domain spanned 122 kilometers. The simulation domain was chosen based on the work of Srinivas et al (2012), who completed their analysis over a distance of 80 kilometers. A larger domain was chosen for the current simulation in order to eliminate boundary condition discontinuities and balance deposition accuracy with computational efficiency.

Figure 3 - 1:6 000 view of hypothetical SMR site (Government of Canada, 2018)

Over the simulation domain land use categories predominantly include forest, populated areas, and water. The topography ranges from 220 meters in height near Centre Lake Junction on the Ontario side of the Ottawa to 120 meters near the river's surface to 420 meters near Pointe à l'Oiseau. Essentially the river follows a shallow valley.

4.2 Meteorological Data (WRF)

Meteorological data from the National Centers for Environmental Prediction (NCEP) were used as the WRF input to generate the meteorological field data for the simulation domain. Specifically, the final Operational Model Global Tropospheric Analyses was used. This data was produced on a grid having mesh dimensions of 1-degree latitude by 1-degree longitude. Data points are produced once every six hours. The WRF simulation generated a datapoint once per hour. For the level of accuracy needed for this study, input data once per six hours was enough to generate adequate wind, pressure, temperature, and humidity data for use by HYSPLIT. The NCEP dataset is maintained current beginning in 1999. The dataset contains 49 fields including temperature, humidity, and wind, among others. The complete list is given in Appendix A.

Data from the operational model was used to generate information about the meteorological field. This information was used as an input to the HYSPLIT dispersion model to determine radionuclide spread and concentration. The data architecture is shown below in Table 4.

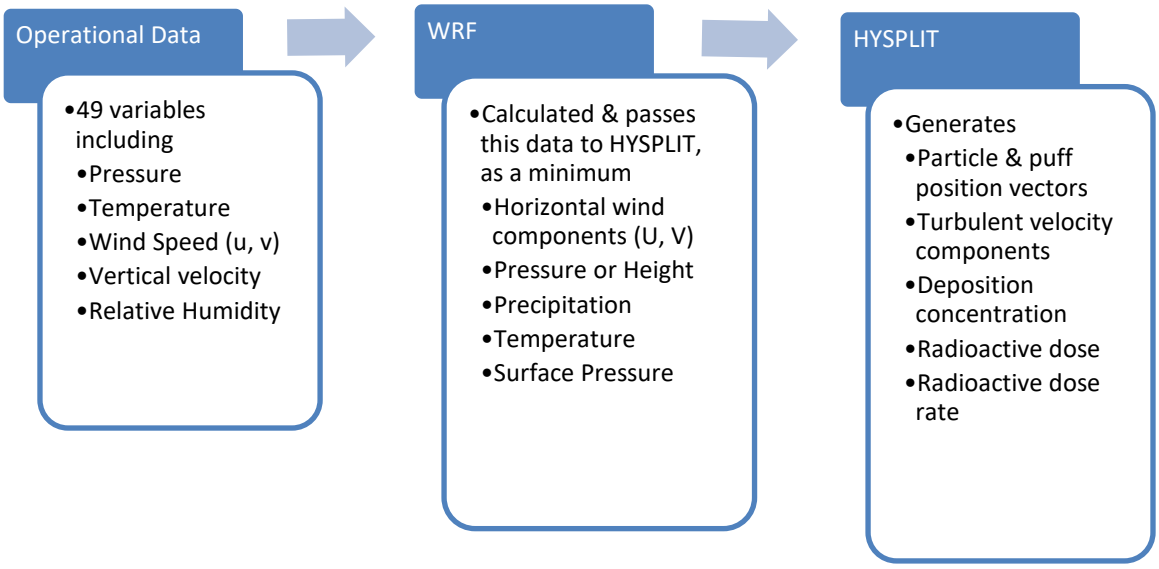

Table 4 – Data Architecture Table Illustrating Parameter Interchange

A time period of April 10, 2017 00:00 hours UTC to April 20, 2017 18:00 hours UTC was chosen as the simulation time period. The work of Srinivas et al (2012) was used to inform the simulation duration selection. Their work used a similar time period and achieved results that were comparable to measurements taken over the same time frame.

Mid-April was chosen since a wide variety of weather is typically experienced in the simulation location at that time of year. It is not unusual to experience a variety of weather conditions in the same day at this time of year. Over the simulation period both rain and clear days occurred. Both windy days and calm days were experienced. This dataset was used to generate meteorological fields using WRF ARW (National Centers for Environmental Prediction/National Weather Service/NOAA/U.S. Department of Commerce, 1997).

4.3 Dispersion Data (HYSPLIT)

The Windows-based graphical version of HYSPLIT was used to analyze radiological concentration, trajectory, dose rate, and total dose. One very useful feature of the HYSPLIT graphical interface is its seamless, direct integration with a number of datasets. The application itself allows you to connect to the data and transfer it in a pre-formatted form that can be consumed by HYSPLIT without any pre-processing.

HYSPLIT was run with two meteorological datasets for this study to provide a method of comparing the dispersion code results. One dataset was generated by WRF. The second, comparison dataset, was the NCEP North American Regional Reanalysis (NARR) data. This data was produced on a 32 kilometer grid and is updated every three hours. The grid size is approximately one-third the size of the FNL dataset used with WRF. This dataset contains information on 85 fields including pressure, temperature, humidity, precipitation, and wind. The entire list of parameters is given in Appendix A (National Centers for Environmental Prediction/National Weather Service/NOAA/U.S. Department of Commerce, 2005).

The HYSPLIT model's grid can be set up to use polar, Mercator, or lambert conformational geographical systems with the intention that the HYSPLIT geographical system is the same as the geographical input data. Vertically, HYSPLIT is able to perform computations with vertical position given in pressure relative to sea level, pressure relative to surface, a combination of these two, and terrain following height. HYSPLIT uses a quadratic equation to establish data resolution with increasing height. The data resolution may be changed by the user with the only restriction being that the model resolution should be the same or better than that of the input data (Draxler and Hess, 2018).

In order to analyze dispersion, HYSPLIT computes particle (or puff) advection and combines the result with a random term meant to account for atmospheric turbulence. This approach is simple. However the random term is implemented through use of a random number generator that may not always generate numbers that are truly random. HYSPLIT uses a hybrid approach to calculate dispersion whereby particle dispersion analysis is calculated in the vertical direction while puff dispersion analysis is carried out in the horizontal direction.

4.3.1 Particle dispersion

Particle motion is calculated by the HYSPLIT code in order to determine particle trajectories and species' concentration in the modelled domain. HYSPLIT uses a combination of vertical diffusivity, wind shear, and horizontal wind to complete the calculations. Trajectory calculations use advection only in order to determine particle travel paths. Particle position due to advection is denoted by P, which can be further split into horizontal components, X & Y, and a vertical component, Z (Draxler and Hess, 2018). Concentration calculations use both advection and turbulence components in order to determine species concentration. Particle position, when being simulated in order to determine the concentration field, is given by X in the horizontal and Z in the vertical.

The dispersion effect of atmospheric turbulence utilizes boundary layer stability to estimate friction velocity and temperature. The friction velocity is a measure of drag while the friction temperature is the value obtained by dividing the sensible heat by the friction velocity. The friction velocity, u*, can be calculated in one of two ways. The first – used when surface fluxes have been calculated by the meteorological model – is given by,

$$u_* = \left(\frac{[\rho C_D u]u}{\rho}\right)^{0.5}, \quad (13)$$

where C_D is the drag coefficient (Draxler and Hess, 2018). The numerator of this equation is a stress term. The second method is,

$$u_* = \left(\frac{|-\boldsymbol{F}|}{\rho}\right)^{0.5}, \quad (14)$$

where **-F** is the vector momentum fluxes in Newtons per square meter (Draxler and Hess, 2018).

The Obukhov length is used by the model to determine vertical and horizontal mixing coefficients, which are used to determine diffusivity in the boundary layer. This requires that the boundary layer depth be known and the user may choose one of four ways to find the depth. Boundary layer depth may be calculated by the meteorological model, estimated from the temperature, calculated from the total kinetic energy, or set to a constant value by the user. HYSPLIT has a built-in feature if the user selects a method for which the required information is not available in the input data. Missing data will result in HYSPLIT estimating depth using temperature profile automatically (Draxler and Hess, 2018).

Advection requires meteorological wind speed input data, either from WRF output data or the NARR data. A first-guess position is calculated using initial release position (user defined) with the velocity vector from the meteorological data to determine final position of the particles each time step.

Particle position, P(t), is reduced to a function of time only in the HYSPLIT code by taking the average of the three-dimensional velocity vectors.

$$\vec{P}'(t + \Delta t) = \vec{P}(t) + \vec{V}(P, t)\Delta t, \quad (15)$$

$$\vec{P}(t+\Delta t) = \vec{P}(t) + 0.5\left[\vec{V}\left(\vec{P},t\right) + \vec{V}\left(\vec{P}',t+\Delta t\right)\right]\Delta t, \quad (16)$$

Specifically, for particle trajectory calculations in HYSPLIT, the position vector components are broken into horizontal and vertical components. Draxler and Hess (2018) give the equations for X component of horizontal velocity. Their equations have been extended to include the Y component as well. Z is the vertical component of the position vector.

$$X_{final}(t+\Delta t) = X_{mean}(t+\Delta t) + U'(t+\Delta t)\Delta t G, \quad (17)$$

$$Y_{final}(t+\Delta t) = Y_{mean}(t+\Delta t) + V'(t+\Delta t)\Delta t G, \quad (18)$$

$$Z_{final}(t+\Delta t) = Z_{mean}(t+\Delta t) + W'(t+\Delta t)\Delta t Z_{top}^{-1}, \quad (19)$$

where G and Z_{top} are unit conversion factors, U', V', and W' are turbulent wind components. The turbulent wind components are determined separately from the particle motion due to advection.

The turbulent wind components, U', V', and W', are modelled using the equations below. The equations are a function of the Lagrangian time scale, T_{Lw}, time step Δt, gradient of velocity variance σ_w, and a random component used to represent turbulence U'', V'', W''(Draxler and Hess, 2018).

$$U'(t+\Delta t) = R(\Delta t)U'(t) + U''(1-R(\Delta t)^2)^{0.5}, \quad (20)$$

$$V'(t+\Delta t) = R(\Delta t)V'(t) + V''(1-R(\Delta t)^2)^{0.5}, \quad (21)$$

$$\frac{W'}{\sigma_w}(t+\Delta t) = R(\Delta t)\frac{W'(t)}{\sigma_{w(t)}} + \frac{W''(t)}{\sigma_{w(t)}}(1-R(\Delta t)^2)^{0.5} + T_{Lw}\left(1-R(\Delta t)\right)\frac{\partial \sigma_{w(t)}}{\partial z}, \quad (22)$$

where the random components – U'', V'', and W'' – are given by $\sigma_i \lambda$ where σ_i is the standard deviation of turbulent velocities and λ is a random number from a Gaussian distribution having a mean of 0 and a standard deviation of 1 (Draxler and Hess, 2018). Turbulent velocity standard deviation is calculated using, $\sigma_i = \left(\frac{K_i}{T_{li}}\right)^{0.5}$, where K_i is the vertical or horizontal diffusivity and T_{li} is a time factor equal to 100 seconds for the vertical direction and 10 800 seconds for the horizontal direction (Draxler and Hess, 2018).

In the equations above, an 'autocorrelation factor', R, is introduced. This factor is a function of the size of the time step. R is given by (Draxler and Hess, 2018),

$$R(\Delta t) = e^{\left(\frac{-\Delta t}{T_{li}}\right)}, \tag{23}$$

The equation for W' is valid when the gradient of the velocity variance, σ_w, is non-zero. In the case of the HYSPLIT model, this term is used to keep particles from building up in areas of low turbulence and skewing results. The gradient of velocity variance is given by the equation

$$\sigma_w(t + \Delta t) = \sigma_w(t) + W'(t)\Delta t \frac{\partial \sigma_w(t)}{\partial z}, \tag{24}$$

where W'(t) is the turbulent velocity in the vertical direction at the end of the last time step (Drexler and Hess, 2018).

The equation for σ_w was developed by Legg and Raupach (1982). Their work endeavoured to show that flows with non-zero vertical velocity gradients could be represented by a modified-Markov equation derived from a Langevin equation. Their motivation lay in the fact that the diffusion equation, while able to be used to accurately calculate dispersion in the atmosphere, cannot be used close to the source or in a vegetation array. Research prior to the

work by Legg and Raupach had identified that measured particle trajectory compared well with a Markov sequence. A simple Markov equation, however, didn't work for flows within vegetation because of high turbulence intensity and irregular velocity profiles (Legg and Raupach, 1982).

Legg and Raupach began with the Langevin equation and a Markov sequence. The Langevin equation is,

$$\frac{dw}{dt} = -\alpha w + \lambda\xi(t), \tag{25}$$

where w(t) is particle vertical velocity, $\alpha=1/T_L$, $\lambda = \sigma_w \frac{\sqrt{2}}{T_L}$, and ξ is Gaussian white noise. They began with Markov sequence $\{w_n\}=\{w(t_n)\}$. Ensuing terms of the Markov sequence are,

$$w_{n+1} = aw_n + b\sigma_w\xi_n, \tag{26}$$

where w_n and w_{n+1} are successive terms in a stochastic process (which turbulence is), ξ_n is a random number from a Gaussian distribution having a mean of 0 and a standard deviation of 1, $a = e^{\frac{-\Delta t}{T_L}}$, T_L is the Lagrangian time scale, $b = (1-a^2)^{\frac{1}{2}}$. Note that this equation is true while $T_\lambda \ll \Delta t \ll T_L$, where T_λ is the time parameter associated with the Taylor microscale (Legg and Raupach, 1982).

Using the Eulerian momentum equation,

$$\frac{\partial \bar{u}_i}{\partial t} + \bar{u_j}\frac{\partial \bar{u}_i}{\partial x_j} + \frac{\partial}{\partial x_j}\overline{u_i' u_j'} = -\frac{1}{\rho}\frac{\partial \bar{p}}{\partial \bar{x}_i} + \nu\nabla^2\bar{u_i}, \tag{27}$$

where u is the Eulerian velocity vector, x is the position vector, p is pressure, ν is kinematic viscosity, and ρ is density. An overbar is used to indicate an average and a prime is used to

indicate a fluctuation (Legg and Raupach, 1982). The vertical component of this equation, re-written in terms of $w_{E,}$ is,

$$\frac{\partial \overline{w\prime_E^2}}{\partial z} = -\frac{1}{\rho}\frac{\partial \bar{p}}{\partial z}. \tag{28}$$

This shows that whenever there is a vertical velocity gradient, there is a pressure-induced force in the vertical direction. In this case the Langevin equation becomes,

$$\frac{dw}{dt} = -\alpha w + \lambda\xi(t) + \frac{\partial}{\partial z}\overline{w'^2_E}, \tag{29}$$

(Legg and Raupach, 1982). This equation is solved and its solution compared with the Markov sequence,

$$w_{n+1} = aw_n + b\sigma_w\xi_n + c, \tag{30}$$

in order to determine that

$$c = \frac{\partial}{\partial z}\overline{w'^2_E}T_L\left(1 - e^{\frac{-\Delta t}{T_L}}\right), \tag{31}$$

(Legg and Raupach, 1982). Comparing the equations for $\frac{dw}{dt}$ and w_{n+1}it can be seen that a Markov sequence can be derived from the Langevin equation. Legg and Raupach's results showed that the mean drift velocity, $\bar{w}$, is $T_L\frac{\partial}{\partial z}\overline{w'^2_E}$. Further, they proved, using simulations, "that a uniform concentration profile [was] preserved" (Legg and Raupach, 1982).

4.3.2 Puff dispersion

Puffs are clouds of particles whose motion in space are approximated as if the cloud were a particle. In contrast to the multi-step calculations used to determine particle dispersion, puff

dispersion is relatively straightforward – requiring computation only of turbulent velocity variances, puff growth, and puff splitting. Velocity variances are computed in the same manner as for particles.

Puff growth rate is determined based on the size of the puff relative to the meteorological grid scale. Puffs that are larger than the grid size are presumed to have been resolved by the meteorological model. For puffs smaller than the grid size vertical and horizontal growth are determined separately. Vertically, growth is given by

$$\frac{d\sigma_z^2}{dt} = 2\sigma_w^2 T_L, \tag{32}$$

where the left hand side is the growth rate of the puff, T_L is the Lagrangian time scale, and σ_w is the puff vertical growth constant. Horizontally, puff growth rate may be defined in one of two ways: linear with time or proportional to the square root of time. The equations for the two options are:

$$\frac{d\sigma_h}{dt} = \sigma_u, \tag{33}$$

$$\frac{d\sigma_h}{dt} = \sigma_u \left(0.5 \frac{T_L}{t}\right)^{0.5}, \tag{34}$$

where the left hand side is the puff growth rate, σ_u is the standard deviation of the turbulent eddies in the horizontal direction, T_L is the Lagrangian time scale, and t is time. The above equations are solved to determine σ_h and σ_z (Draxler and Hess, 2018).

As in the vertical direction, turbulence velocity variance is determined using the same approach as for particle dispersion calculations. This is a key defining parameter of how the puffs move in response to atmospheric turbulence. With the velocity variance known, the turbulent velocity component can be calculated for the current time step. The change in turbulent

velocity and mean velocity terms due to Δt is calculated and the terms added to give velocity at the end of the current time step.

In order to prevent a puff from growing to a size that would cover a substantial portion of the geographical domain HYSPLIT uses puff splitting to limit puff size relative to grid spacing. In the vertical direction, all puffs are assumed to be 'top-hat' puffs. A 'top-hat' puff is one with a constant concentration inside the puff. Outside the puff, the species' concentration is zero. When σ_z grows to be 1.54 times the size of the grid spacing the puff is split into four separate puffs – each having one-quarter of the mass of the original puff. In the horizontal, puffs may be 'top-hat' or Gaussian. Within a Gaussian puff, species' concentration is distributed following a Gaussian distribution. 'Top-hat' puffs in the horizontal direction split in exactly the same manner as described for the vertical direction. Gaussian puffs split into five smaller puffs, as opposed to four for the 'top-hat' puff, when three times the value of σ_h is greater than the model grid size.

With splitting, puff volume can grow to a size that would exceed the size of the computational domain. To prevent this from happening HYSPLIT is equipped with three methods to remove puffs. These are: 1) merging puffs whose centres are close together every hour, 2) merging lightweight puffs every six hours, and 3) applying a 'maximum' puff age criterion. While useful to prevent unrealistic increases in concentration as puffs accumulate and overlap in the domain, it would be interesting to understand if these mechanisms also lead to under-reporting of the dispersion concentration.

Calculation of species concentration within a puff varies depending on whether the puff is a 'top-hat' or Gaussian puff. The incremental concentration contributed to the whole by each

puff is calculated and then summed each time step to give a complete distribution. Incremental concentration equations for 'top-hat' and Gaussian puffs, respectively, are given by

$$\Delta c = m(\pi r^2 \Delta z)^{-1}, \tag{35}$$

$$\Delta c = m(\pi r^2 \Delta z)^{-1} e^{-0.5\frac{x^2}{\sigma_h^2}}, \tag{36}$$

where Δc is the incremental concentration of an individual puff, m is mass, r is the horizontal puff radius, $r = 1.54\sigma_h$, x is the distance from centre of the puff to the grid point used for concentration summing, and Δz is the vertical extent, $\Delta z = 3.08\sigma_z$ (Draxler and Hess, 2018). The 'top-hat' puff concentration is calculated much more simply than the Gaussian while the Gaussian calculation method is more exact. The accuracy of the Gaussian method comes with a higher computational cost.

4.3.3 Deposition

HYSPLIT includes three different mechanisms that result in species deposition. These include: wet deposition, dry deposition, and radioactive decay. Wet and dry deposition are calculated using the following equation,

$$D_{wet+dry} = m\left\{1 - e^{[-\Delta t(\beta_{dry}+\beta_{gas}+\beta_{inc}+\beta_{bel})]}\right\}, \tag{37}$$

where $D_{wet+dry}$ is total deposition due to wet and dry mechanisms, m is the pollutant mass, Δt is the time step, β_{dry} is the time constant for dry deposition, β_{gas} is wet scavenging for gases, β_{inc} is in-cloud wet removal for particles, and β_{bel} is below cloud wet removal for particles (Draxler and Hess, 2018).

Dry deposition employs particle settling velocity in order to determine deposit location. Key inputs used to compute the velocity are diameter and density of the particles under consideration.

Gravitational settling is a special case of dry deposition that includes air density and particle density in determining the settling rate (Draxler and Hess, 2018). HYSPLIT uses resistance factors for each of the atmosphere's sublayers to determine overall settling velocity,

$$V_d = \frac{1}{R_a+R_b+R_c+R_aR_bV_g} + V_g, \tag{38}$$

where V_d is settling velocity, R_a is resistance due to the atmospheric layer, R_b is resistance due to the laminar sublayer, R_c is resistance due to vegetation canopy, V_g is gravitational settling velocity (Draxler and Hess, 2018). The settling velocity is used to determine the dry time constant,

$$\beta_{dry} = V_d \frac{1}{\Delta Z_p}, \tag{39}$$

where ΔZ_p is the depth of the pollutant layer. For puffs, this equals $1.54\sigma_z$. For particles, this is simply the surface layer depth (Draxler and Hess, 2018).

Wet deposition is defined using a "deposition velocity" (Draxler and Hess, 2018). For particulate species this involves use of the scavenging ratio and precipitation rate. HYSPLIT uses a different settling time constant depending on whether the species of interest is in cloud or below cloud. The in-cloud time constant is,

$$\beta_{inc} = F^t F_b V_{inc} \Delta Z_p^{-1}, \tag{40}$$

where F^t is the pollutant fraction below the cloud top and F_b is the pollutant fraction above the cloud bottom. V_{inc}=SP where S is the average scavenging ratio and P is the precipitation rate. Typically the scavenging ratio varies from 5×10^{-5} to 1×10^{-6} (Draxler and Hess, 2018). Below cloud scavenging is given by,

$$\beta_{bel} = 1 \times 10^{-6}(1 - F_b). \quad (41)$$

For gases, scavenging depends on solubility – defined by the Henry's Law constant. Calculating the scavenging rate for gases is a little more involved than for particulate since the gaseous deposition velocity also depends on temperature, precipitation, and the universal gas constant. The time constant for gases is,

$$\beta_{gas} = F^t V_{gas} \Delta Z_p^{-1}, \quad (42)$$

where deposition velocity, V_{gas}=HRTP, H is the Henry's Law constant, R is the universal gas constant, and T is temperature.

Radioactive decay, while not a deposition mechanism in and of itself, is treated similarly to deposition in that a time constant is calculated. The time constant, β_{rad}, is given by the following equation,

$$\beta_{rad} = ln \frac{2}{T_{\frac{1}{2}}}, \quad (43)$$

where $T_{1/2}$ is the half life of the pollutant species. Radioactive 'deposition' is then calculated using,

$$m_2 = m_1 e^{-\beta_{rad} \Delta t}, \quad (44)$$

where m_1 is mass of the radioactive pollutant calculated in the last timestep, m_2 is the current mass of the radioactive pollutant, and Δt is the time step (Draxler and Hess, 2018).

In addition to these three mechanisms, HYSPLIT includes a sub-routine that allows for re-dispersal of deposited material. Re-dispersal occurs when force due to wind speed at the surface exceeds the forces holding the material to the surface. The resuspension flux is given by,

$$\frac{dS}{dt} = ku_*KS, \tag{45}$$

where S is the amount deposited on the surface, K is the pollutant concentration in air divided by S, ku* is atmospheric resistance (Draxler and Hess, 2018).

The impact of radioactive decay on deposition concentration uses the half-life of the species under consideration along with the model time to calculate isotope concentration. From the concentration, given in Bequerels per cubic meter of air above ground level, dose rate and total dose is determined directly (Draxler and Hess, 2018).

In this study, all of the deposition methods were used to calculate dose rate and total dose at ground level & 10, 500, 5 000, and 8 000 meters above ground level (AGL).

4.3.4 HYSPLIT Model Validation

While HYSPLIT has been subjected to experimental validation, the code has some limitations. One such limitation is that of radioactive decay is calculated as if the decay begins at the time the particles are released. In actuality, decay processes begin as soon as the isotope is formed. The time between isotope formation in the reactor core and its release following a reactor accident varies depending on reactor design, nuclear fuel type, and operating conditions. This is a source of uncertainty and potentially overestimates the quantity of radioisotopes deposited in the dispersion path (NOAA, undated).

This overestimation may be inconsequential since dose to the public will be very high following large releases and the additional dose due to uncertainty will be negligible; small releases – those that are well within regulatory requirements – will be more conservative in that the calculated dose will be higher than actual dose. The uncertainty will be impactful only when the release amount results in an anticipated dose close to the regulatory limit. In Canada, nuclear facilities are required to demonstrate they operate well within regulatory limits. An operating nuclear facility could not obtain an operating licence without including the uncertainty if the anticipated release was close to the limit. The only way to know is to compare model results with measurements. This sounds simple. It can be difficult to accurately quantify the impact on model results since there are several sources of uncertainty (e.g. meteorological wind field uncertainty, precipitation uncertainty, source term uncertainty) and each is difficult to quantify. A possible approach could be to couple statistical models for each uncertainty source. This is beyond the scope of the current study.

Chapter 5
Results & Discussion

5.1 Meteorological Fields

The key fields generated by WRF included wind speed, wind direction, temperature, water vapour, cloud water, and precipitation amounts. Input data with a resolution of 30 arc-seconds was used to simulate fields on a model grid spacing of one kilometer and a domain measuring 148 kilometers in the West-East dimension and 122 kilometers in the North-South dimension. A single domain was used to analyze wind and precipitation using a Lambert map projection. A map projection is used to position calculated dispersion within the HYSPLIT grid cells such that the positioning is accurate in comparison to the spherical shape of the Earth. Projections are used to eliminate distortion that occurs when translating position on a sphere to an analysis domain. A Lambert projection is shown in Figure 4.

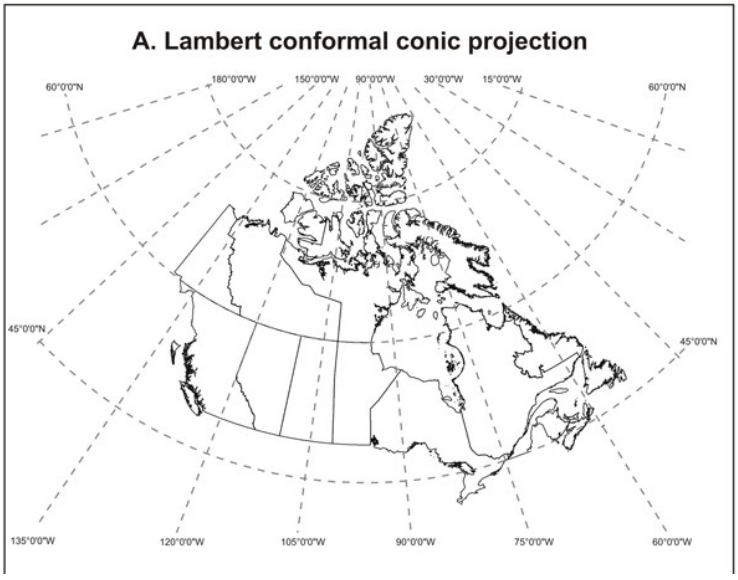

Data points were output once each hour. WRF was run over a ten-day period from April 10 to 20, 2017. Data was analyzed to qualitatively determine the impact of wind direction, height, and precipitation on radionuclide dispersion.

Figure 4 - Statistics Canada, 2018

In Figures 5 through 11 the terrain height, in meters, is shown as a contour plot. Wind speed and direction at a terrain height of 10 meters are given by the vector arrows. Arrow colouring is used to show speed in meters per second. Figures 11-14 show rainfall and wind velocity.

5.1.1 Terrain Height and Wind Velocity

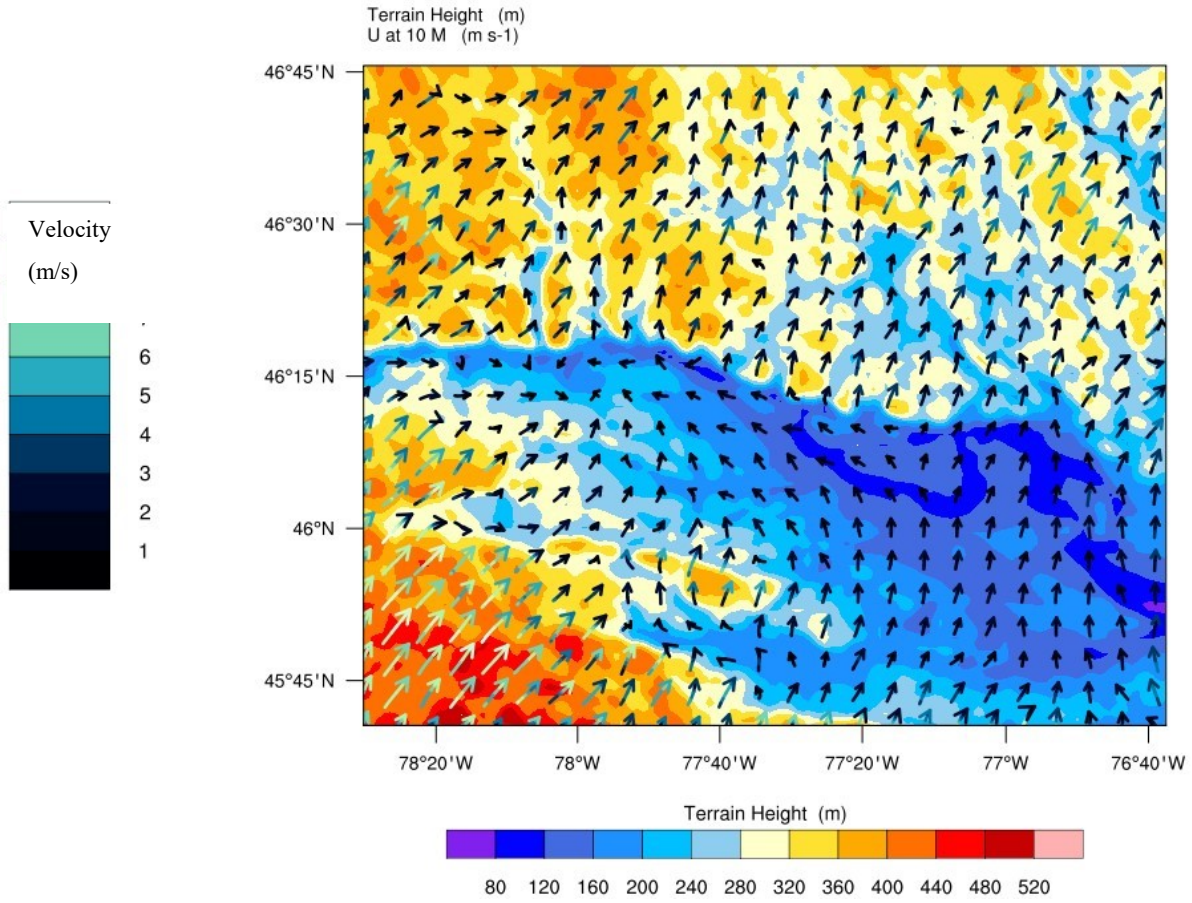

Figure 5 – Velocity field at the time of first radionuclide release; 10APR2017 0100 hrs GMT Terrain height (contour plot) and wind speed, direction (vectors)

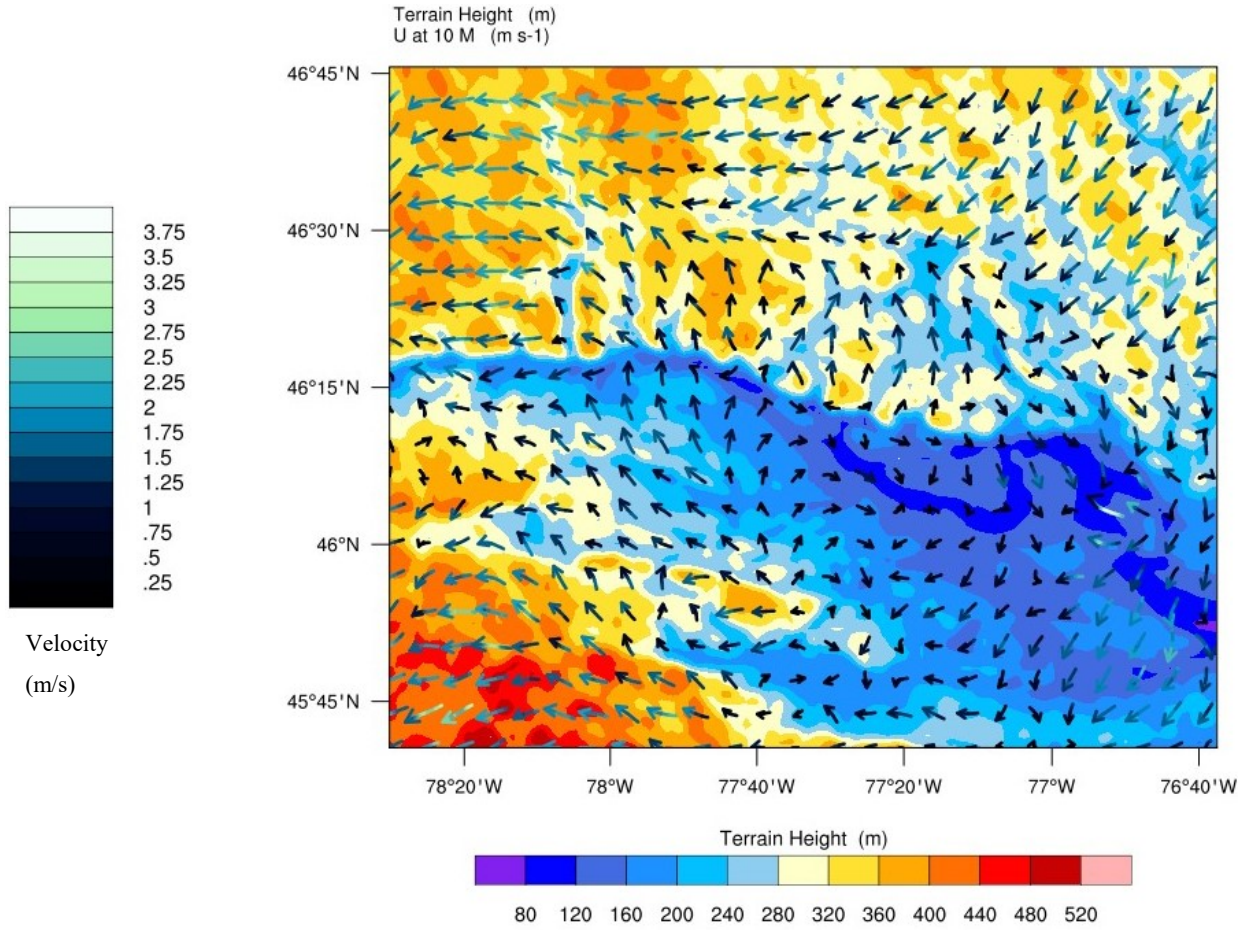

Figure 6 - 20APR2017 0100 hrs GMT Terrain height (contour plot) and wind speed, direction (vectors)

As can be seen from Figure 7 wind direction can change rather drastically day-to-day. The two plots show wind directions varied by up to 180 degrees in the 24-hour period beginning April 11th, 2017 at 01:00 hours. This variation continues throughout the study period from April 10th to 20th. Plots showing the winds over this period are shown in pairs below.

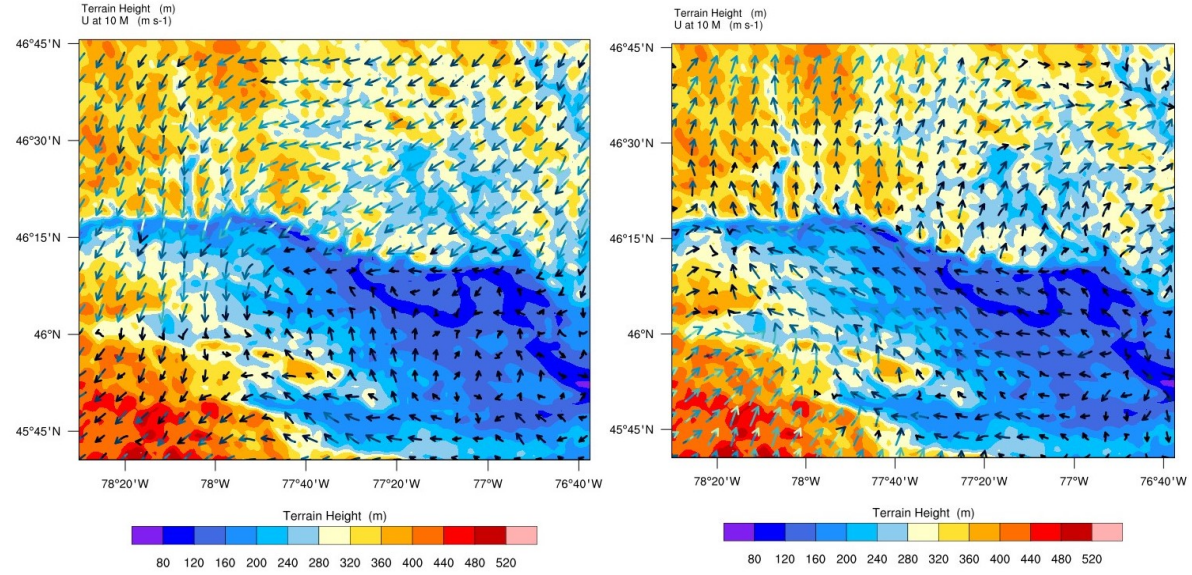

Figure 7 - Wind speed and direction; 11APR2017 0100 hrs GMT (left) and 12APR2017 0100 hrs GMT (right)

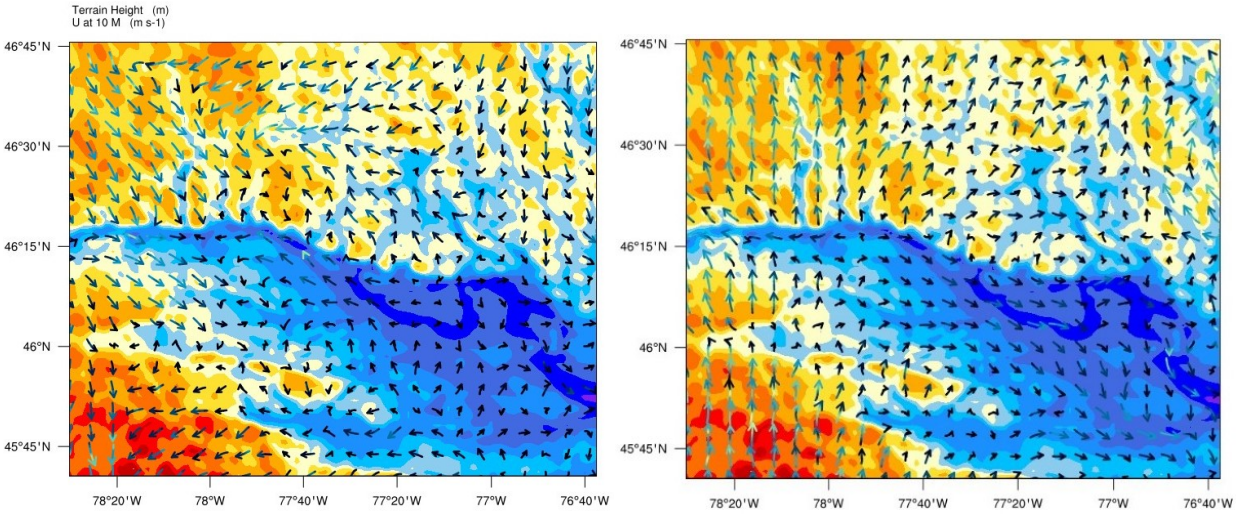

Figure 8 – Wind speed and direction; 13APR2017 0100 hrs GMT (left) and 14APR2017 0100 hrs GMT (right)

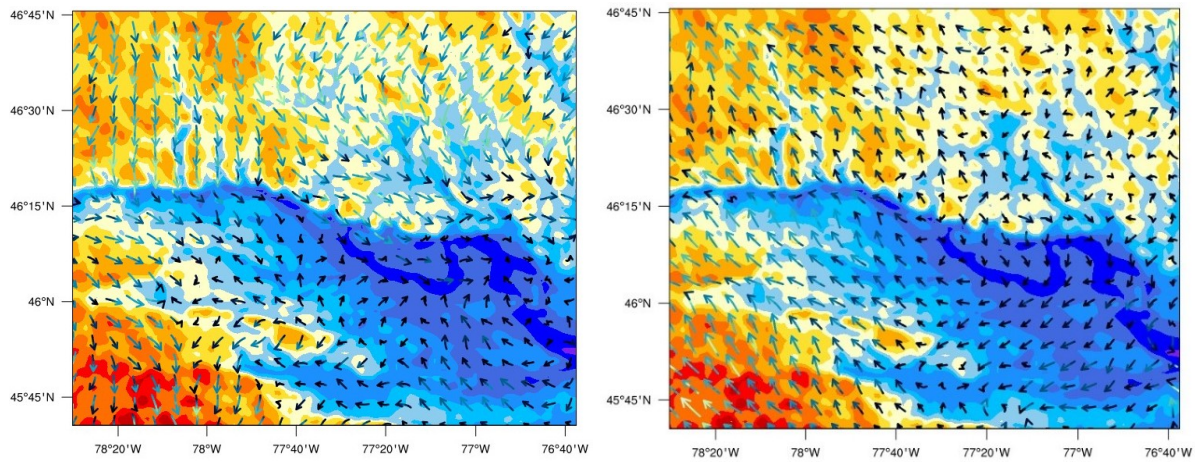

Figure 9 - Wind speed and direction; 15APR2017 0100 hrs GMT (left) and 16APR2017 0100 hrs GMT (right)

Wind direction appears to shift direction in a 24-hour cycle from April 13th to 16th – ranging from North-West and South on the 13th and 14th, respectively, to North and South-East on the 15th and 16th.

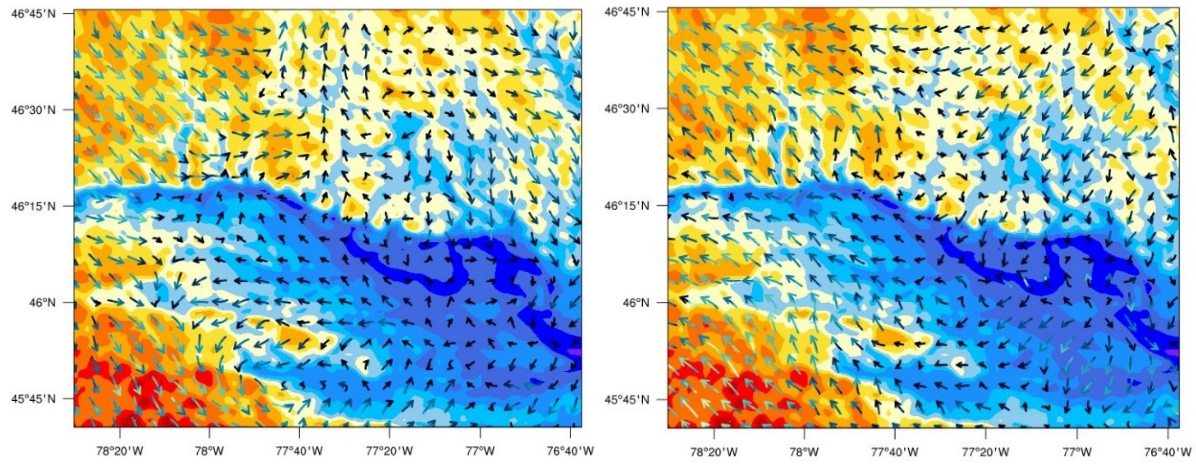

Figure 10 - Wind speed and direction; 17APR2017 0100 hrs GMT (left) and 18APR2017 0100 hrs GMT (right)

Over the ten-day simulation period the wind direction changes outside the river valley. Inside the river valley, however, wind direction differs substantially from the direction outside the valley. It is interesting to note that air flow direction was not always the same upstream and downstream of the valley. In the simulation domain terrain height is higher to the southwest and northwest of the Ottawa River than to the northeast. The Ottawa River fills the southeast corner of the simulation domain. It had been expected that wind speed would always be highest at the highest elevation. That expectation did not hold entirely true. Wind speed was highest at elevations between 360 and 520 meters, but on several occasions wind speed was higher at 360 meters than at 520 meters. Wind speed was consistently lowest at the lowest elevation over the Ottawa River. Wind speed at the elevation of the river was generally at or below 1 meter per second. On the final day of simulation, April 20th, wind speed in the further south east corner of the model domain reached speeds up to 2.75 meters per second.

5.1.2 Precipitation

It was anticipated that rainfall would have an impact on how quickly radioisotopes, with the exception of the nobel gas Xenon-133, would deposit at ground level. What was not anticipated is the very strong impact of not having any rainfall at the time the release occurred. Figure 11 shows that at the release start time, 01:00 hours on April 10th, rain rate is 2.5×10^{-5} millimeters per hour and calculated precipitation was much less than 1 millimeter. Essentially, there was no precipitation during this time period. As will be seen later in the concentration and dose calculations, this lack of moisture has an impact on the extent of radioactive cloud travel.

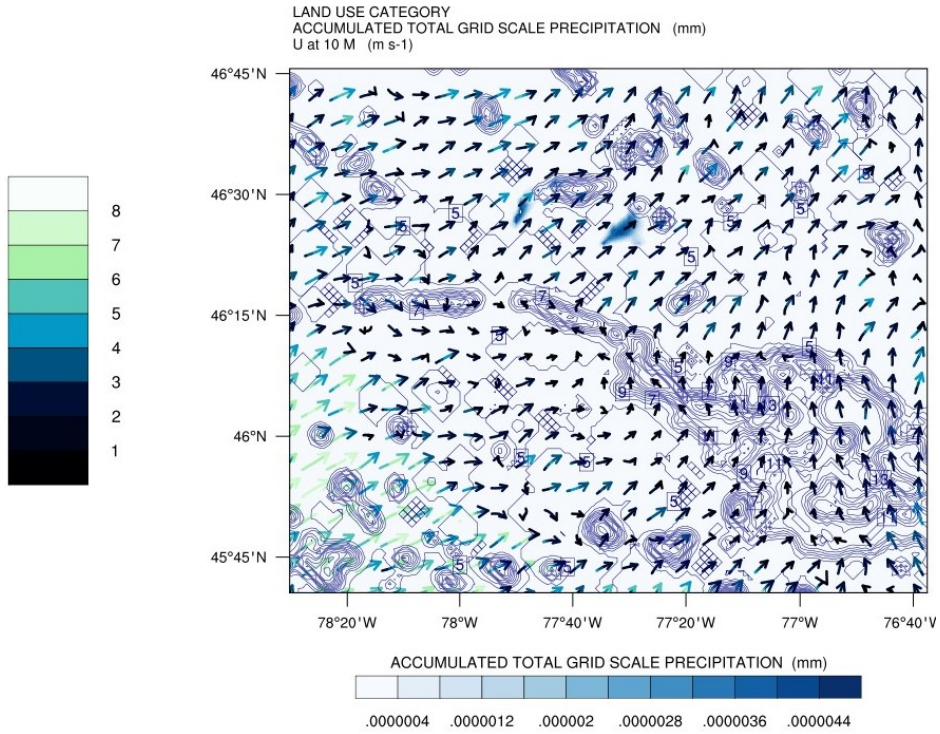

Figure 11 - 10APR2017 0200 hrs GMT; Cumulative rainfall (millimeters) and wind direction one hour after the radioactive release began; Land use is shown as a line contour plot to highlight the location of the Ottawa River

As can be seen from Figure 11, wind is coming strongly from the South-West one hour after the radioactive release begins. Because there is essentially no rainfall at this time, the release cloud moves to the North-East. Dry deposition is the dominant mode of radionuclide settling.

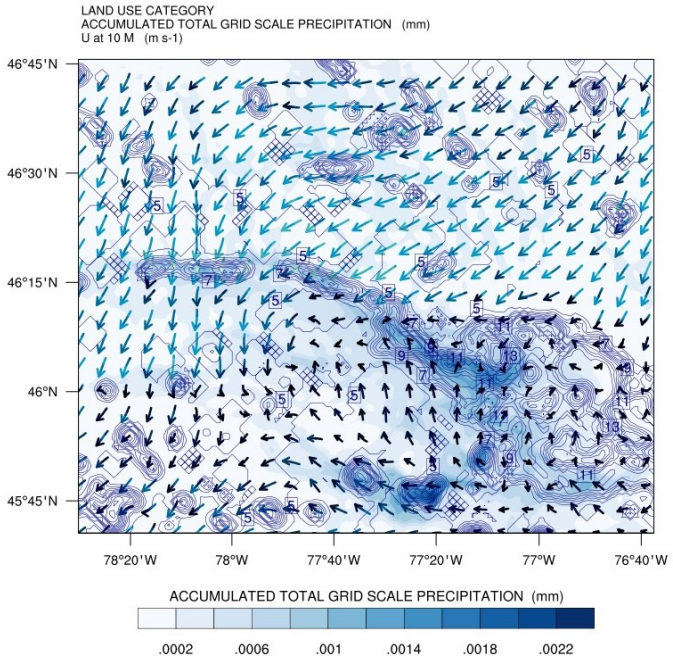

Figure 12 - 11APR2017 0100 hrs GMT; Cumulative rainfall (mm) and wind direction 24 hours after radioactive release began

Twenty-four hours after the radioactive release began wind direction has shifted to the North-East. The radioactive cloud, it would be expected, would be pushed back toward the source of the initial release. This expectation will be analyzed further in the next section, dispersion fields.

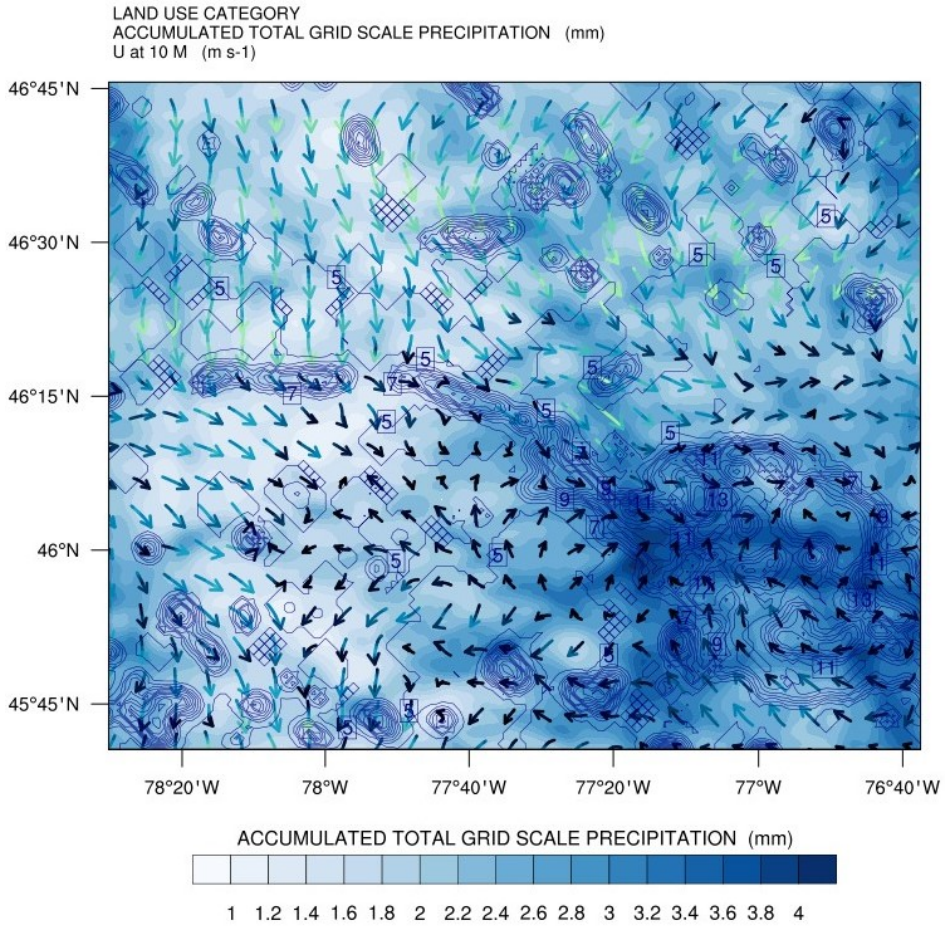

Figure 13 - 15APR2017 0100 hrs GMT; Accumulated rainfall (mm) and wind direction, magnitude

By April 15th, rain has begun to accumulate. By this time, however, the radioactive cloud would have already dispersed such that people and the environment are being exposed to adverse effects.

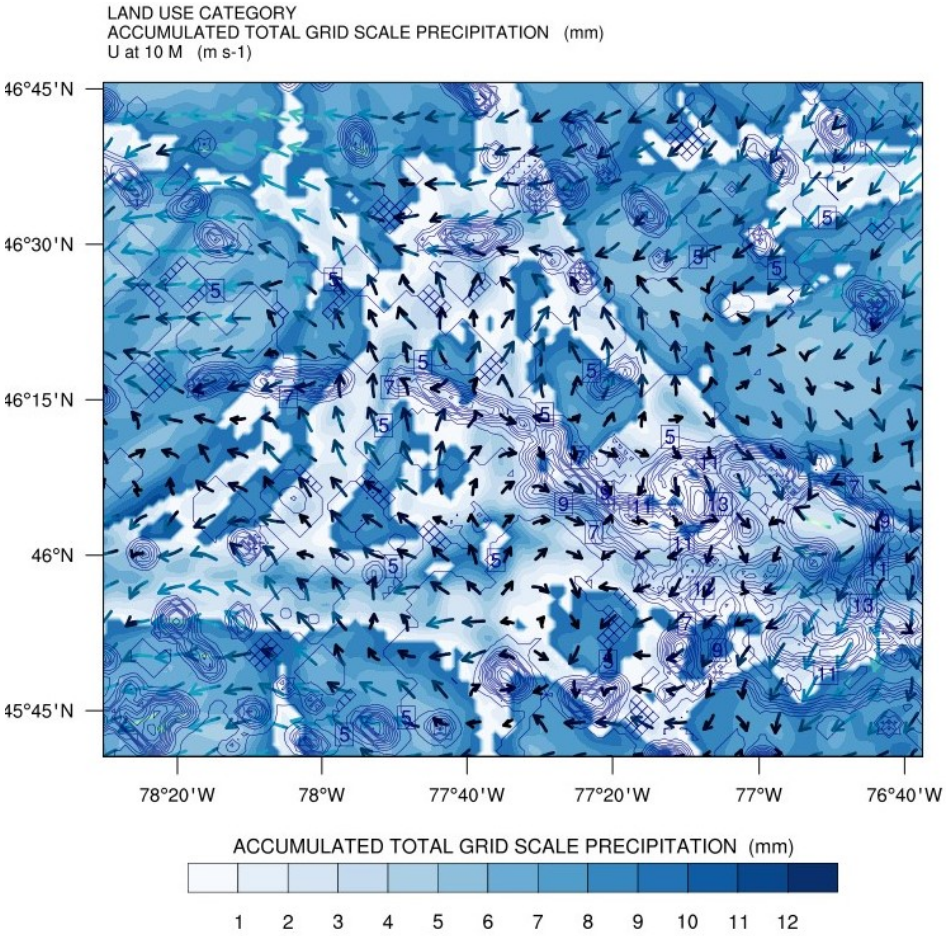

Figure 14 - 20APR2017 0100; Accumulated rainfall at the end of the simulation with wind direction and magnitude

By the end of the simulation period on April 20th rainfall has accumulated up to 10 millimeters in some areas.

The impact of the rainfall later in the simulation appears to have a much lesser effect on dose to people and the environment. Because the assumption implicit in the source term is that a large amount of radionuclide is released, it is unlikely that people living in the dispersion path would benefit from any dilution during mass transfer processes during the dispersion period

selected for this study. Even a small percentage of the released amount would still result in a high dose rate. This is further discussed in the next section.

It is noted that this result is simply one of many possible outcomes since precipitation will vary drastically over time. In order to gain insight regarding the impact of precipitation, simulations over a variety of time periods would be necessary in order to reduce the level of uncertainty in the analysis.

5.2 Dispersion Fields Generated with Reanalysis Data

Dispersion analysis was completed over a domain size of 30.0 degrees latitude and 30.0 degrees longitude with the model SMR located at the centre of the dispersion grid, shown as a red dot in the dispersion figures. The input data used to generate these dispersion figures was reanalysis data rather than the WRF model output. This approach was chosen to provide a set of results for comparison to the dispersion results generated using the WRF output. The dispersion results generated using WRF output are in the next sub-section.

Figure 15 depicts the average concentration of radionuclides between ground level and ten meters above ground. The results are displayed in this manner in Figures 16 to 24 in order to show how much of the pollutants will fall below the release point – which is at 10 meters. Ten meters above ground level was chosen as the top of the first level since, in this first analysis case, the release point is assumed to be located 10 meters above ground. Dose rate and total dose are both calculated between 0 and 10 mAGL since this is where people, animals, and plants are generally located. Dose rate is given in units of millirem per hour since this is a common unit used for nuclear worker radiation exposure. Total dose to the public, as reported by regulatory

agencies, is commonly given in milliSieverts. This study has adopted these units for dose rate and total dose, respectively.

It can be seen that a land area approximately 30 by 90 kilometers to the north-east of the reactor site will have an average radionuclide concentration of 1 x 10^6 Bq/m^3. A larger area, measuring approximately 100 by 300 kilometers, will see an average concentration that is one order of magnitude lower, 10 000 Bq/m^3. Regardless of the order of magnitude decrease, the entire area has an effective dose rate greater than 100 millirem per hour. In SI units this equates to 1 milliSievert per hour. To put this number into perspective, the Canadian dose limit prescribed for members of the public on an annual basis is 1 milliSievert per year (Canada, 2018).

These numbers may seem high since it is unusual to have simulation results on the order of 10^{19}. These results are as expected. The driving factor in such high release rates is the amount of radioactive material released. Even a small volume of radioactive material emits a large amount of radiation. The results are comparable to studies by Korsakissok et al (2013), Hu et al (2014), and Morino et al (2011).

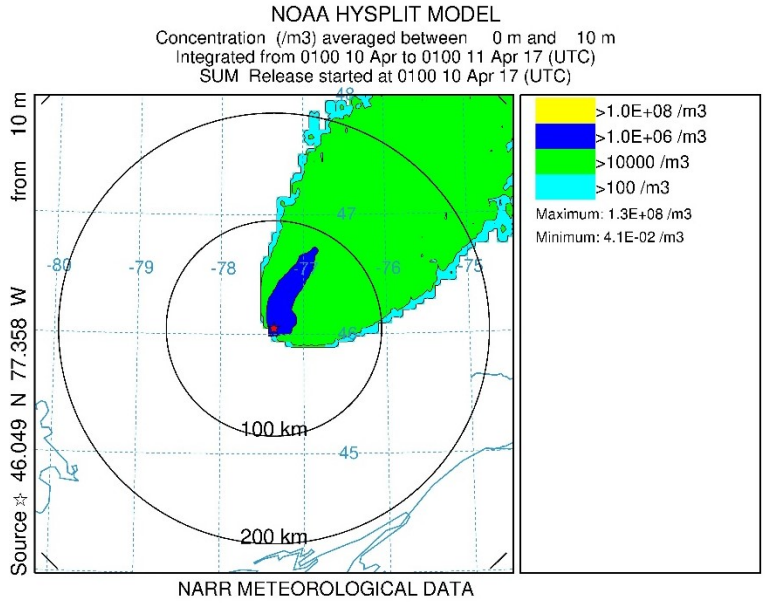

Figure 15 - 20APR2017 Radionuclide concentration averaged between 0 and 10 meters Above Ground Level (AGL)

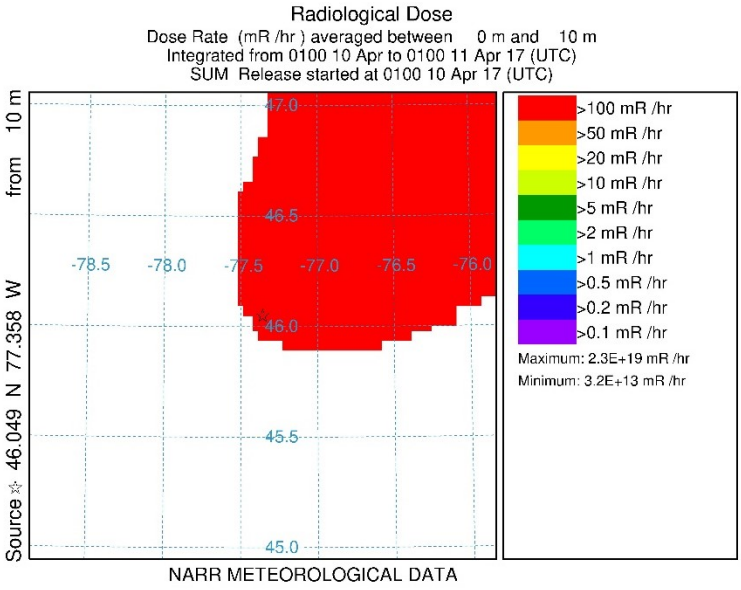

Figure 16 - 20 APR2017 Dose rate in millirem per hour; averaged between 0 and 10 mAGL

The change in radionuclide concentration from 10 meters to 500 meters and from 500 meters to 5 000 meters is shown in Figures 17 and 18. The release point is 10 meters above ground level in each case.

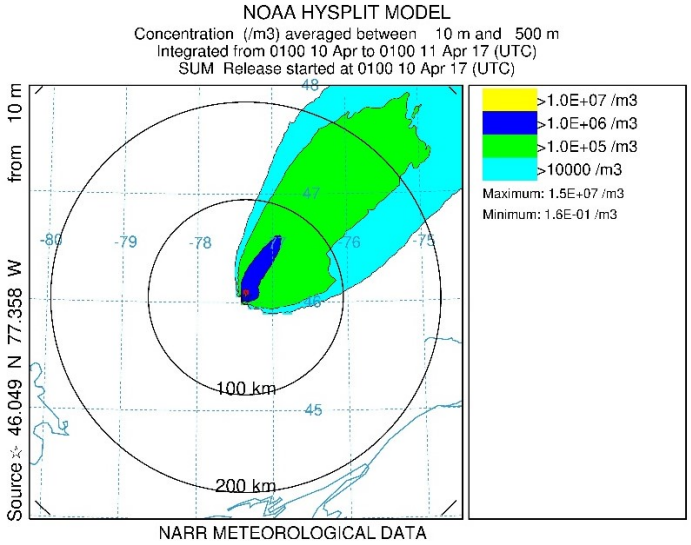

Figure 17 - 20APR2017 Radionuclide concentration averaged from 10 to 500 mAGL; Release at 10 mAGL

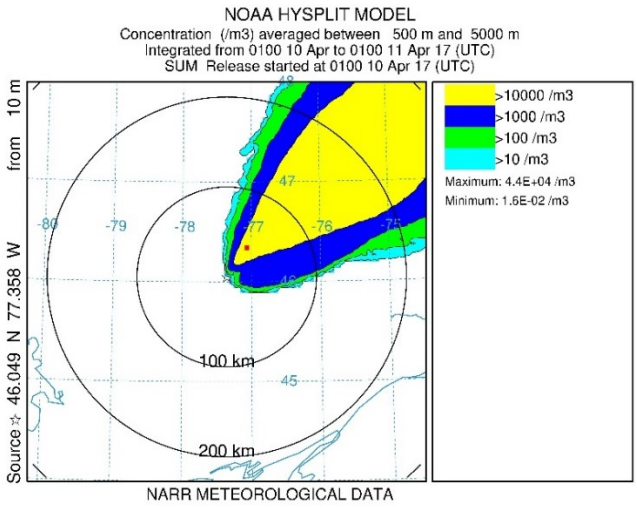

Figure 18 - 20APR2017 radionuclide concentration averaged from 500 to 5000 mAGL; Release at 10 mAGL

The radioactive plume is very similar in shape up to 500 meters. From 500 to 5 000 mAGL, shown in Figure 18, it can be seen that the radionuclide concentration is both higher and more disperse than at ground level. The analysis would seem to suggest that released gases and particulate may go above nearby populations, plants, and animals. However, when pushed to higher levels of the atmosphere pollutants can spread rather extensively before settling.

5.2.1 Comparing a Release at 10 mAGL & 100 mAGL

We can attempt to validate this hypothesis by comparing radionuclide concentration at two different release points: 10 meters and 100 meters. Ten meters was selected on the basis that a small reactor is likely to be 10 meters or less in height above ground level while a postulated explosion could carry particulate and gases 100 meters above ground level.

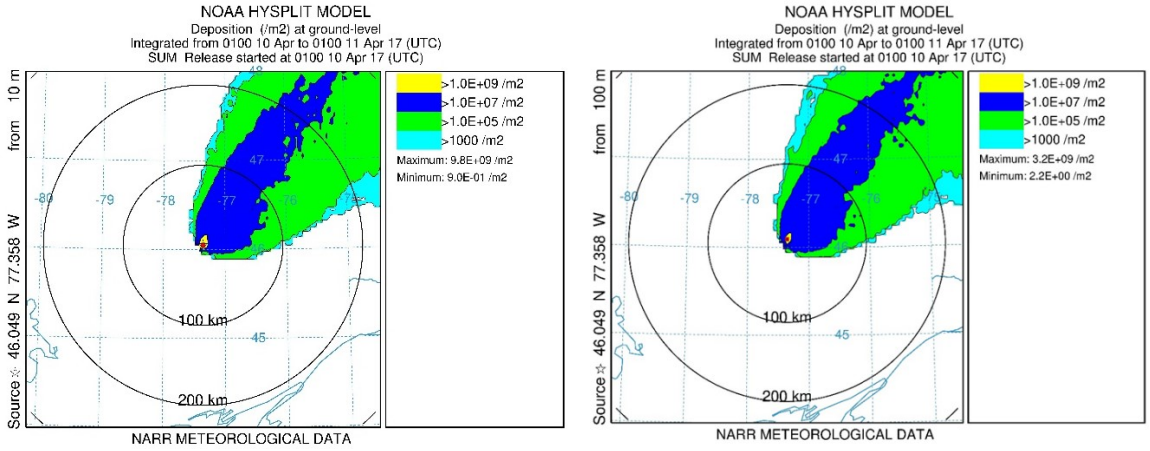

Figure 19 - 20APR2017 0 mAGL; Release at 10 mAGL on the left; Release at 100 mAGL on the right

At ground level the radioactive cloud shape does not appear to be much different regardless of whether pollutants are released at 10 meters or 100 meters about ground. It is expected that this is due to the mean wind speeds in the reanalysis data and the fact there is no precipitation on the early days of the release.

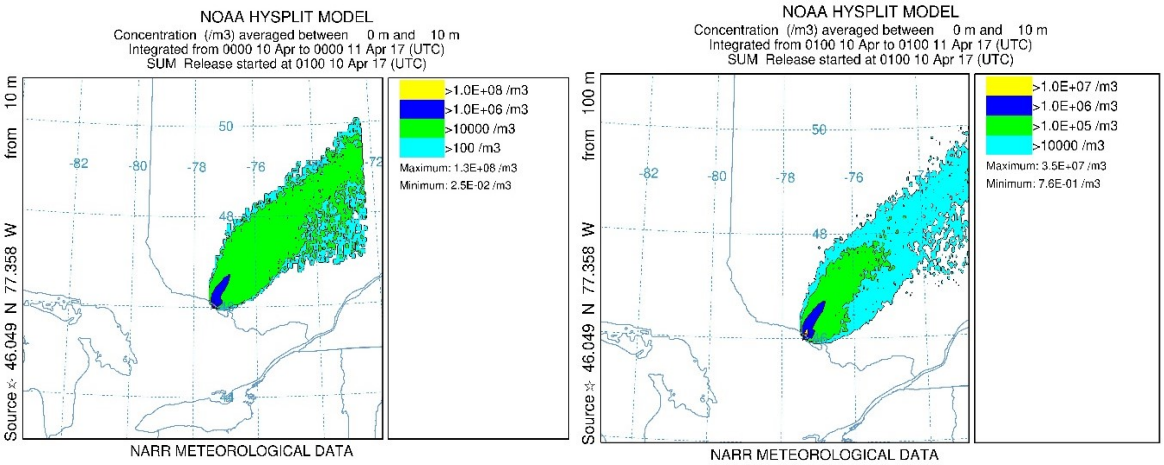

Figure 20 - 20APR2018 10 mAGL; Release at 10 mAGL on the left; Release at 100 mAGL on the right

At 10 meters above ground level, however there is a difference in radionuclide concentrations. At first glance the difference appears to be substantial due to the difference in contours between the two images. Looking at the scale, however, it can be seen that the cloud having a radionuclide concentration of 10 000 Bq/m^3 extends approximately the same distance in both images. For a release point 10 meters above ground level, the extent of the dispersion is greater but the radionuclide concentration is two orders of magnitude lower at the cloud's outer-most edge.

This concentration difference, practically speaking, is not anticipated to have any major benefit for people, plants, and animals in the lower concentration areas since the dose rate and total dose are still high enough to cause adverse health effects. It is most important to analyze dose rate and dose in the 0 to 10 meter range since that is where the bulk of flora and fauna exist. Dose rate and total dose associated with the dispersion in this range was calculated for a release point at 10 meters and 100 meters. At 10 meters, maximum dose rate was determined to be 2.2×10^{19} millirem per hour and maximum total dose was determined to be 5.3×10^{18} milliSieverts. At 100 meters, the maximum dose rate was 6.1×10^{18} millirem per hour while the maximum total dose was 1.5×10^{18} milliSieverts within the simulation domain.

It is prudent to point out that the concentration, dose rate, and total dose calculated by HYSPLIT assume that all radionuclides make their way into the environment and that none of the material is captured by a safety system or other containment method. The practical conclusion from this analysis is that all types of reactors, regardless of size, require design features that prevent radiological releases and offer containment functionality in the event a release does occur.

Moving the release point further up into the atmosphere, from 10 meters to 100 meters, the effect of release does not change substantially. When the release point is higher in the atmosphere, the radionuclide cloud travels a little farther before depositing on the ground. This results in lower doses per person, but there is potential to have more people exposed to radiation that could cause adverse health effects. A hypothesized contributor to this is the low rain rate early in the accident sequence.

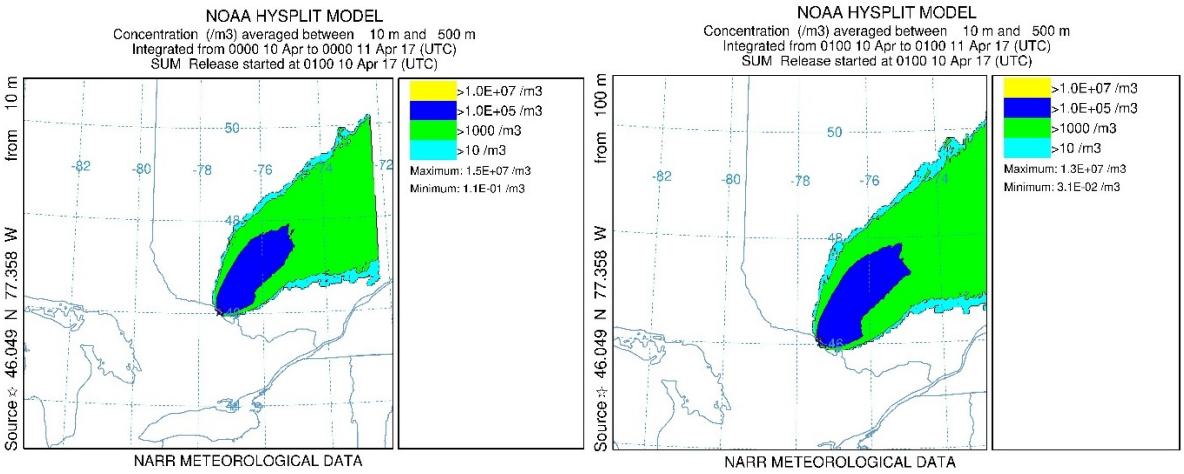

Figure 21 - 20APR2018 500 mAGL radionuclide concentration; Release at 10 mAGL on the left; Release at 100 mAGL on the right

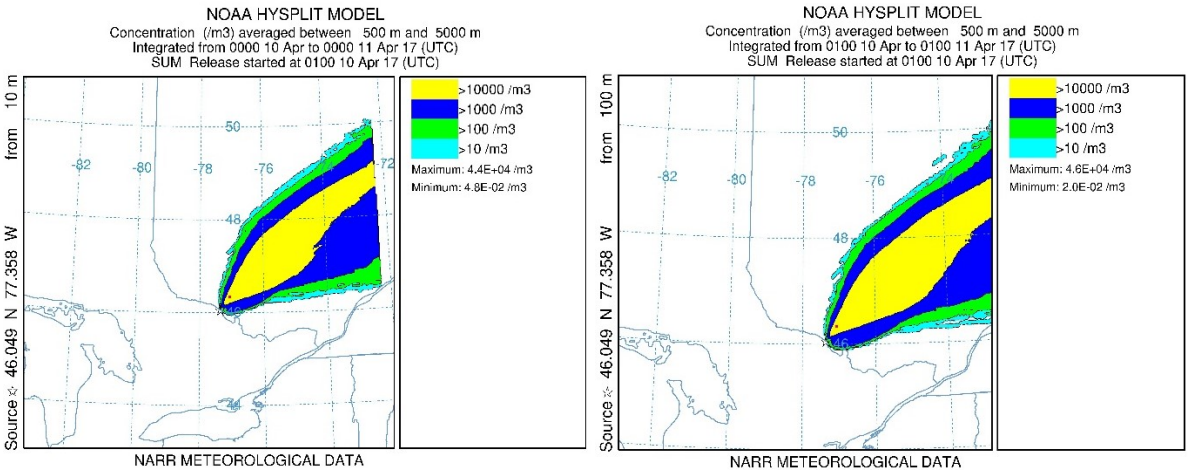

Figure 22 - 20APR2018 5000 mAGL radionuclide concentration; Release at 10 mAGL on the left; Release at 100 mAGL on the right

The extent of radionuclide travel is higher both at 500 meters and 5 000 meters above ground level when the release point is at 100 mAGL rather than 10 mAGL. Radionuclide concentration falls to zero at a height of 8 000 mAGL. If radionuclides were present over 8 000 mAGL global impact due to an accident would be expected. This was the situation following the Chernobyl accident. Having radionuclides stay closer to the ground minimizes the dispersion extent. Perception of this result depends on whether a person lives within the affected area, as dose rates will be higher there, or outside the affected area.

5.2.2 Near-ground Releases

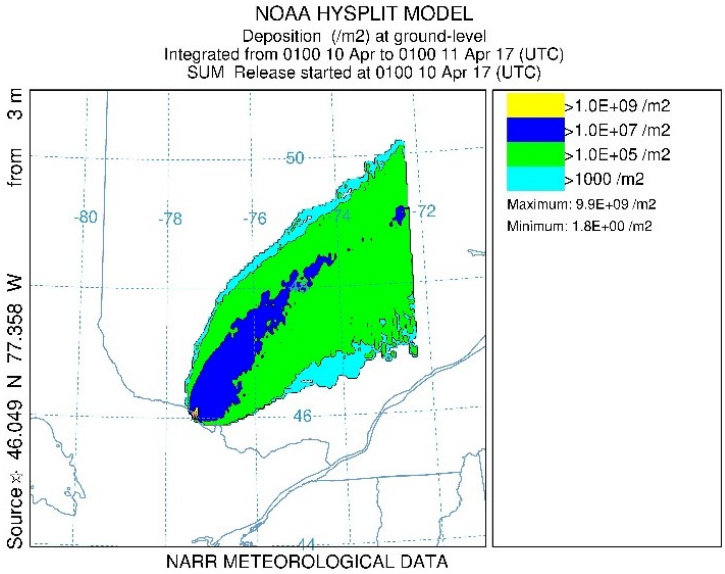

Figure 23 - 20APR2017 Radionuclide concentration at ground level; Release at 3 mAGL

As small modular reactor designs lack a 'typical' layout, a near-ground release was also analyzed for further comparison. Three meters above ground level would encompass releases from research reactor designs and any reactor designs that were built partially or entirely below ground. The results are shown in Figure 23 at ground level. Figure 24 illustrates the change in radioactive plume averaged from 0 to 10 mAGL, 10 to 500 mAGL, and 500 to 5 000 mAGL.

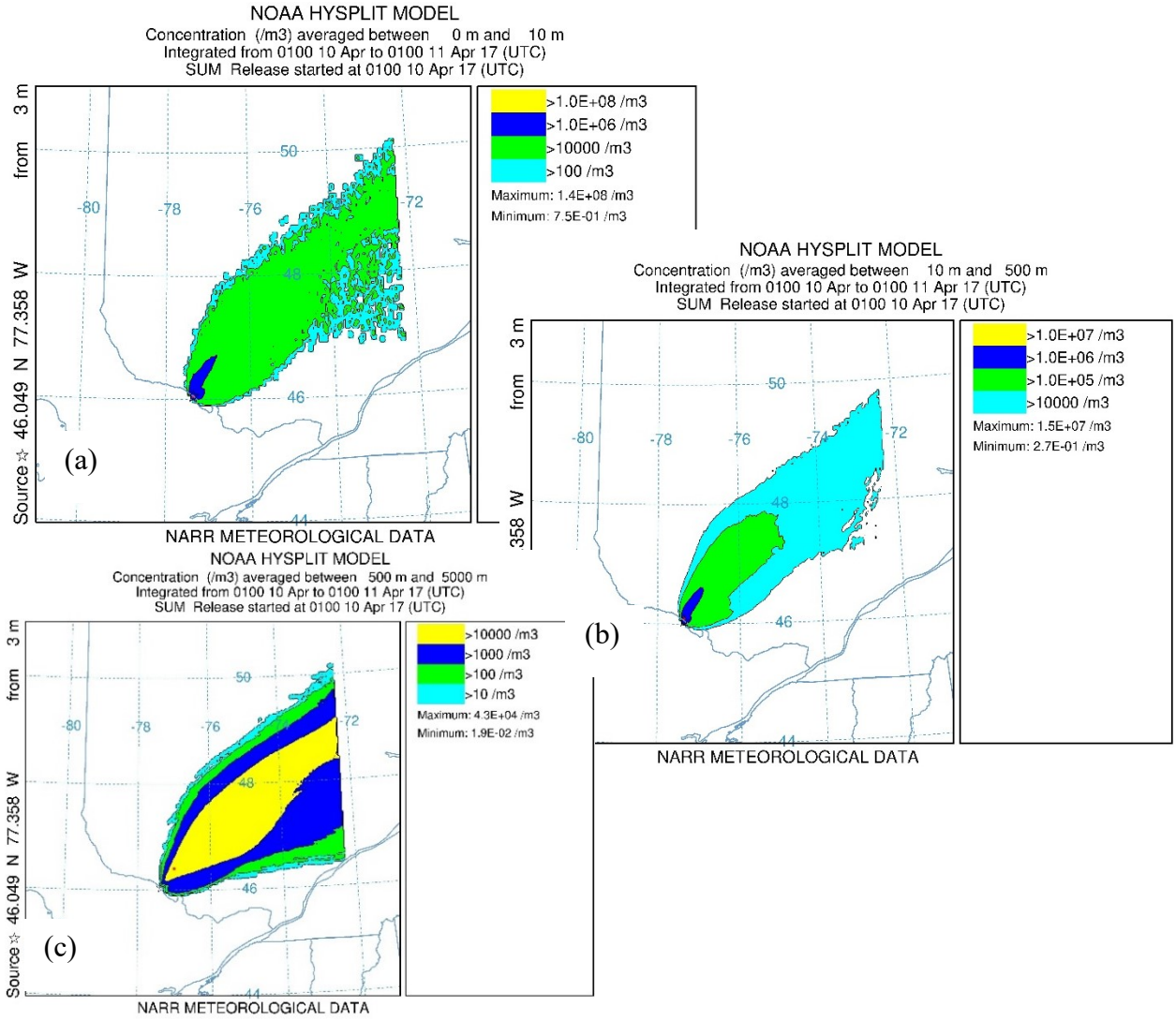

Figure 24 - 20APR2017 Isotope concentration; Panel (a) 0 to 10 mAGL, Panel (b) 10 to 500 mAGL, Panel (c) 500 to 5 000 mAGL; Release at 3 mAGL

Maximum calculated radionuclide concentration, at ground level, for a 3 mAGL release was approximately equal to the 10 mAGL release and approximately an order of magnitude

higher than for the 100 mAGL release. The relationship between release height and concentration near ground level is a linear relationship as shown in Figure 25.

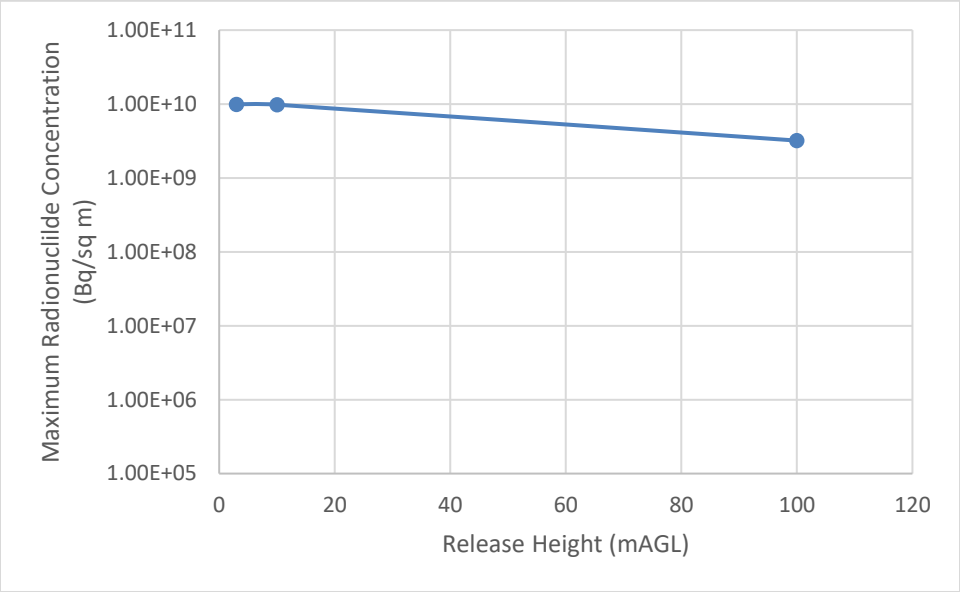

Figure 25 - Release height versus Maximum Radionuclide Concentration at ground level

5.2.3 Release Limit Analysis

Release limit analysis is undertaken for the purpose of establishing an order of magnitude decrease in radionuclide release that would be required to avoid adverse health effects to members of the public following Small Modular Reactor accidents. Studies of Hiroshima and Nagasaki residents in 1945 showed that the primary long-term adverse effect of radiation exposure was an increase in the number of cancers in the exposed population (Canadian Nuclear Safety Commission, 2012).

The methodology for the release limit analysis involved reducing the quantity of radionuclides in the release until concentrations at ground level decreased low enough to meet

the Canadian Nuclear Safety Commission (CNSC) annual limit for dose to a member of the public. This limit includes a safety margin and is set based on studies conducted on populations chronically exposed to radionuclides, such as early uranium miners and residents living near the site of the Chernobyl nuclear accident (Canadian Nuclear Safety Commission, 2012).

According to epidemiological information referenced by the CNSC "studies to date have not been able to show any excess cancers or other diseases in people chronically exposed to radiation at doses lower than about 100 milliSieverts [sic]" (Canadian Nuclear Safety Commission, 2012). Based on this information, and inclusive of a safety factor, the Canadian Nuclear Safety Commission annual limit for exposure to a member of the public as a result of nuclear facility activity is 1 milliSievert. To put this value into perspective dose from a single lung X-ray is approximately 0.1 milliSieverts; the annual dose Canadians receive from natural background sources is about 1.8 milliSieverts. A common source of the Canadian natural background dose comes from exposure to naturally occurring radioactive materials found in the Canadian Shield. A situation some Canadians may have heard of is the presence of Radon gas in home basements. This gas is generated when radioactive materials in the Canadian Shield decay. According to CNSC INFO-0813, Radon and Health, "long-term exposure to above-background levels of radon increases the risk of developing lung cancer" (Canadian Nuclear Safety Commission, 2012). It "has not been linked to other cancers or causes of death" (Canadian Nuclear Safety Commission, 2012).

The initial source term in this analysis included an order of magnitude of 10^{17} for Iodine-131 and Xenon-133. The order of magnitude for Cesium-137 was 10^{15}. A series of simulations was run wherein release amounts were reduced by factors of 1 000, 1 000, 100, and 100.

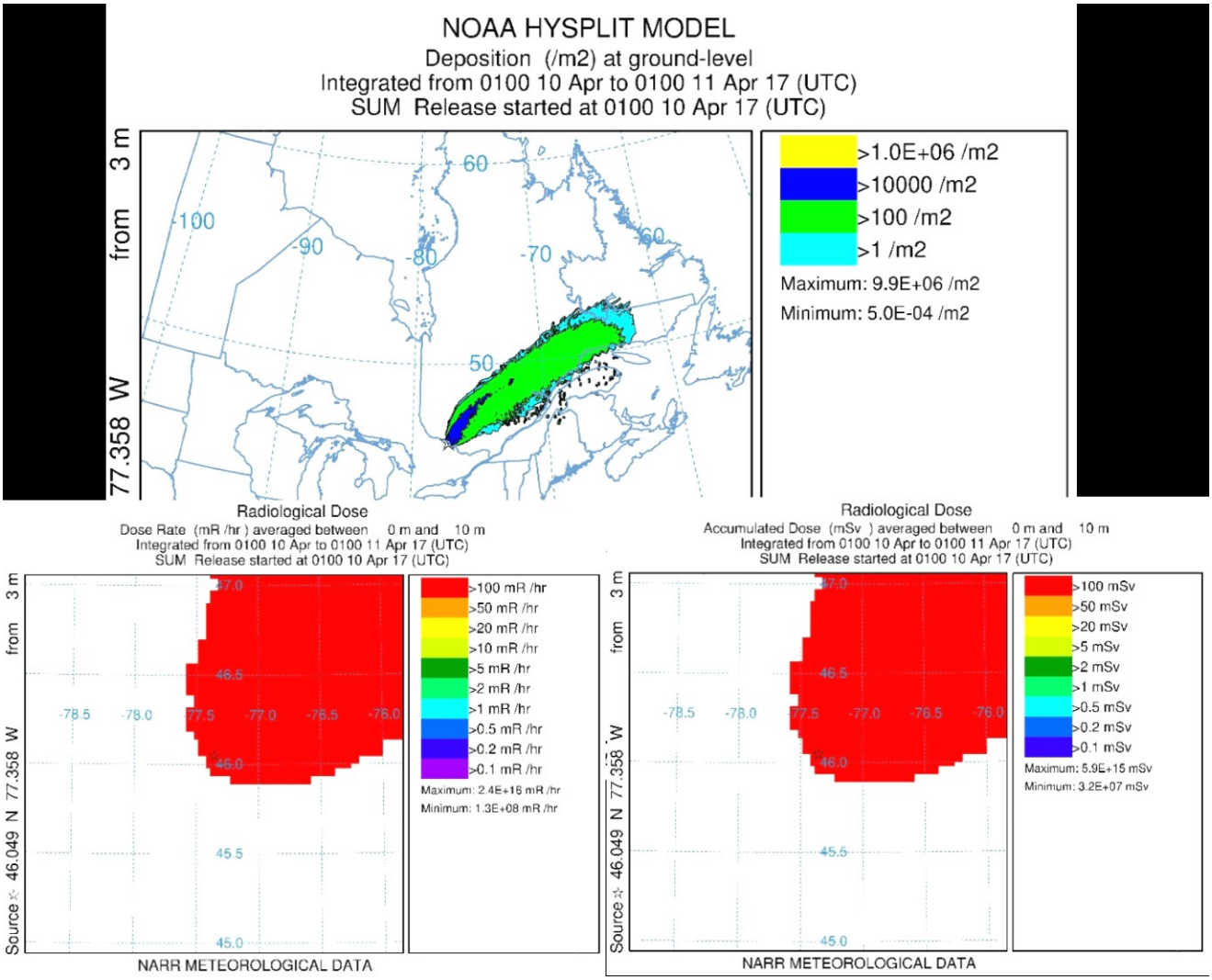

Figure 26 – Deposition concentration, dose rate, and total dose 0.001 times original

The first simulation was run with a radionuclide amount that was 0.001 times the original source term. The results are shown in Figure 26. Maximum dose rate was 2.4 x 10^{16} millirem/hour. Total dose was 5.9 x 10^{15}. While maximum dose rate and total dose decreased the levels are still very high – far too high to be acceptable for release into the environment.

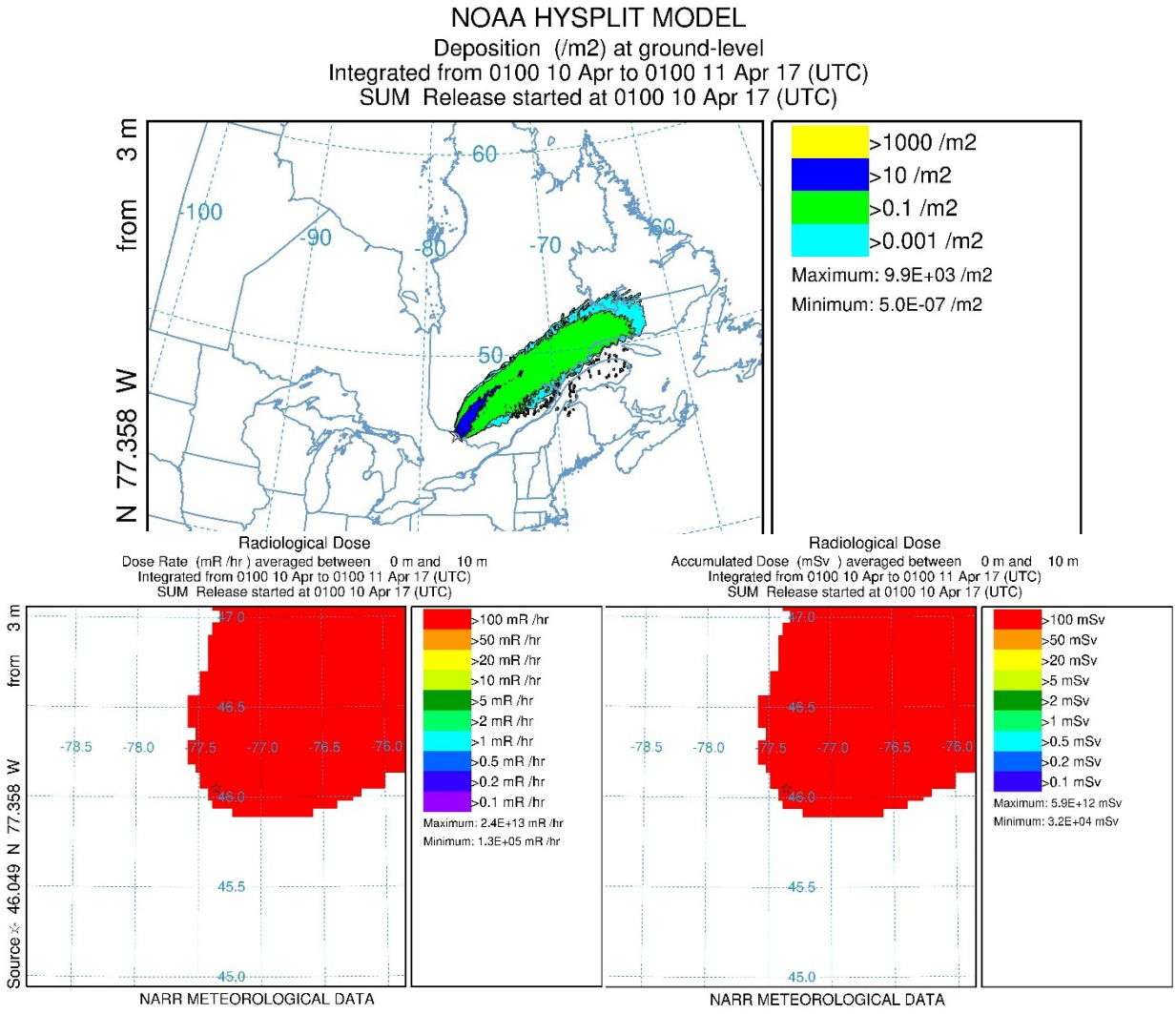

Figure 27 - Concentration, dose rate, and total dose 0.000001 times original

It is noted that a second decrease, by a factor of 100, results in a lower maximum dose and dose rate. The maximum dose rate is 2.4 x 10^{13} millirem/hour and total dose is 5.9 x 10^{12} milliSieverts, as shown in Figure 27. Because the values are still so high, there is essentially no decrease in the impact on plants, animals, and people in the affected area.

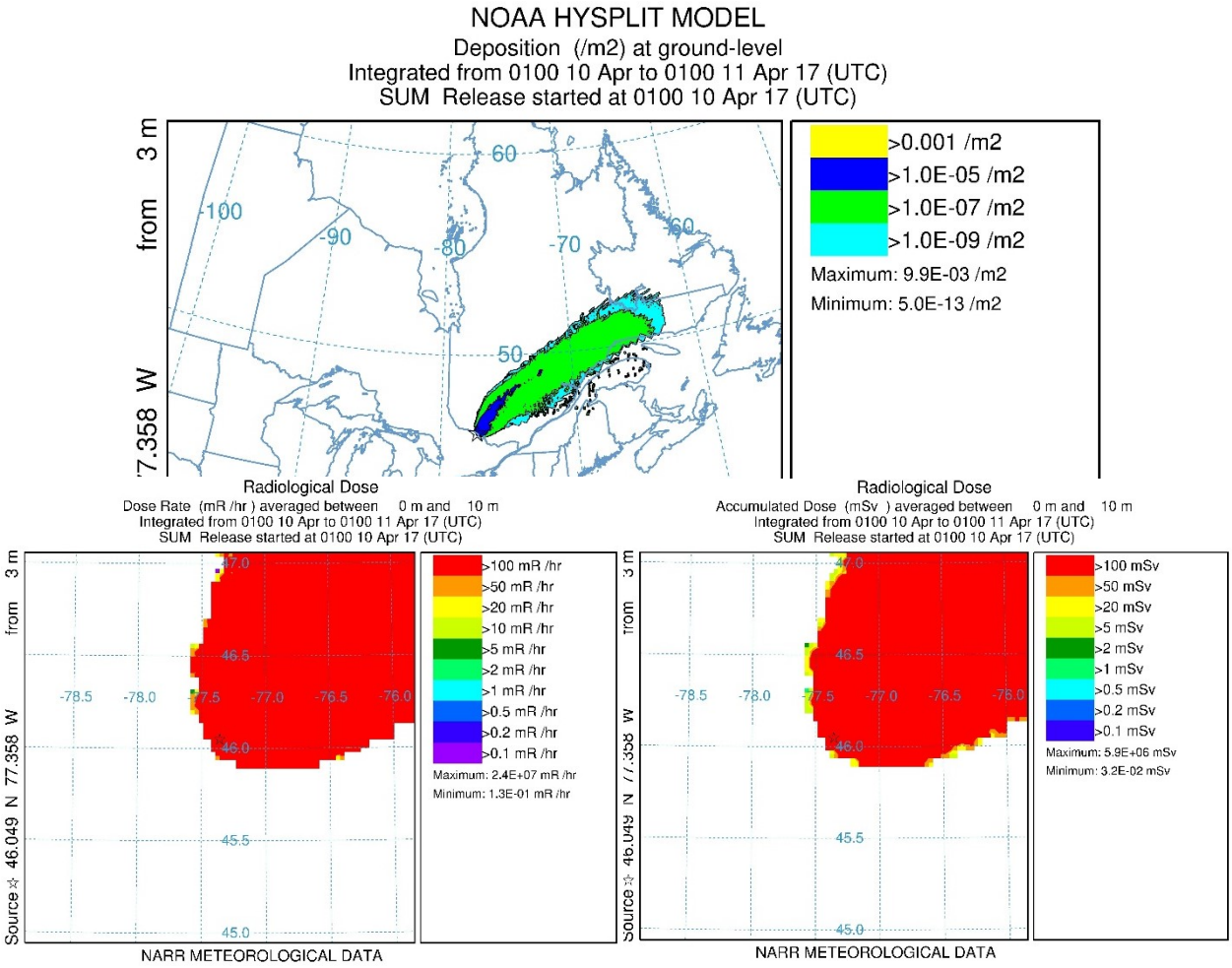

Figure 28 - Concentration, dose rate, and total dose 0.0000000001 times original

Nuclide amount in the release was reduced further, first by a factor of 1 000 and then two susequent decreases by a factor of 100. The release amount after the reductions was 10^{10} times less than the initial source term. It was at this point that dose rate and total dose began to decrease at the extent of the affected area, as shown in Figure 28.

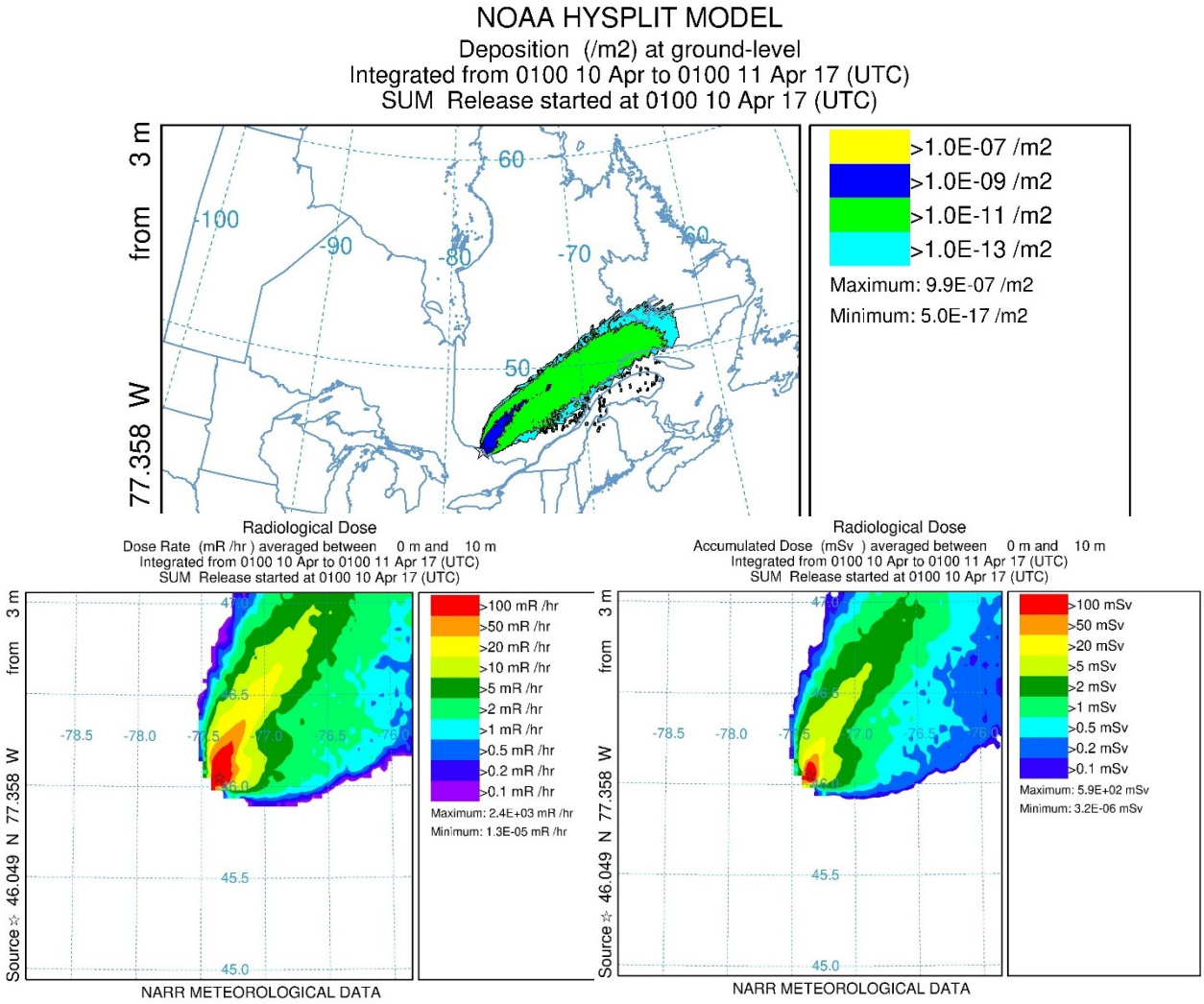

Figure 29 - Concentration, dose rate, and dose 1 x 10^{14} times less than original

At a source term 1 x 10^{14} times less than the original source term both dose rate and total dose had declined to a level that was nearing the point where health effects begin to diminish for most of the affected people, plants, and animals. Figure 29 shows that the population outside an area 50 by 100 kilometers away from the reactor are exposed to a dose amount less than or equal to the CNSC requirement of 1 milliSievert.

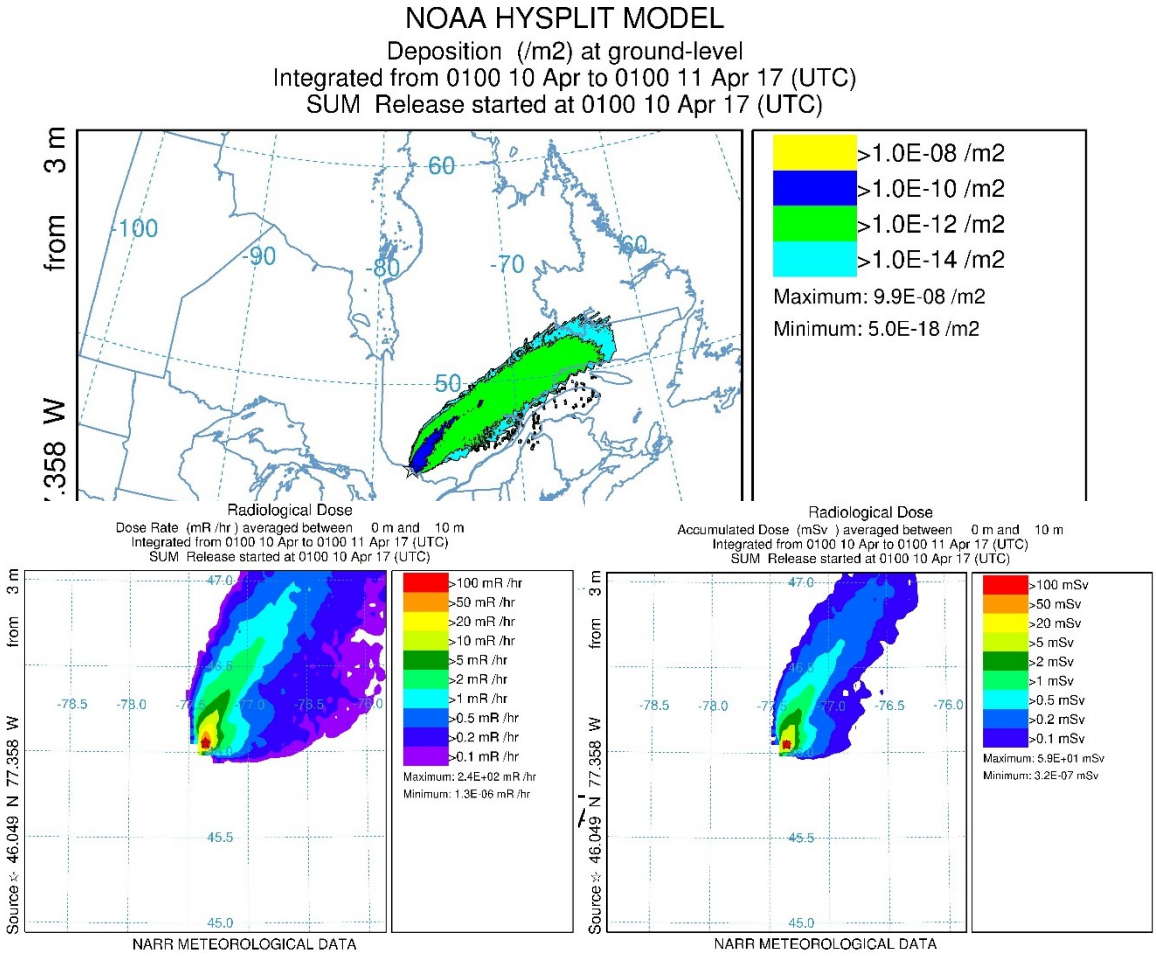

Figure 30 - Concentration, dose rate, and dose 1 x 10^{17} times less than original

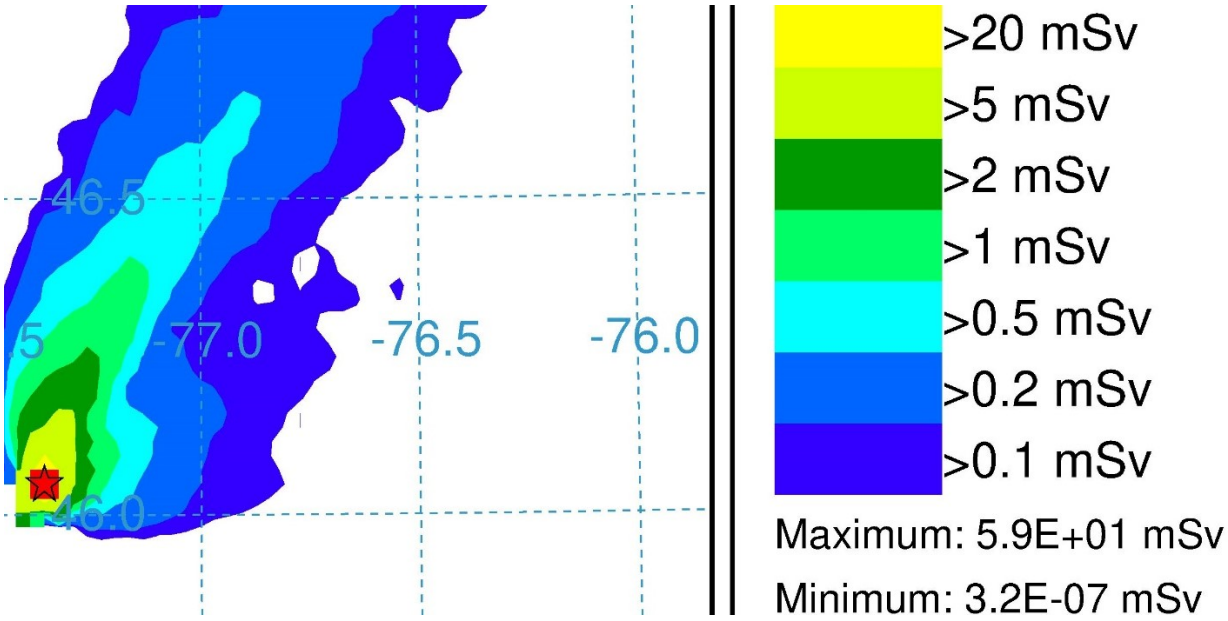

Figure 31 - Magnified view of total accumulated dose; Source term 1 x 10^{17} times less than original

A final simulation was run with a source term 1 x 10^{17} times less than the original source term. The results are shown in Figure 30. Figure 31 shows a magnified view of the total dose surrounding the Small Modular Reactor. From the magnified view it can be seen that dose falls to the CNSC public dose limit within 25 kilometers in the Northerly direction and with 10 kilometers to the West and East of the facility. Further, dose decreases to below the natural background dose within approximately 10 kilometers in all directions. For those right at the facility total dose is calculated to be 59 milliSieverts.

For people at the facility, assumed to be workers there, dose limits are set differently than for the public. The CNSC mandates that such workers be designated as Nuclear Energy Workers (NEW). The annual dose limit for a non-pregnant NEW during facility operations is 50

milliSieverts. At this level, the epidemiological studies support no increased risk of cancers as a result of the exposure. For comparison purposes, it is noted that a person undergoing a whole body Computerized Axial Tomography (CAT) scan receives dose in the vicinity of 30 to 100 milliSieverts (CNSC 2012).

5.3 Dispersion Field Generated with WRF Data

The WRF domain, being 148 by 122 kilometers, spans approximately one degree of latitude and longitude. The WRF domain is a small fraction of the domain used with the reanalysis data – which spanned thirty degrees of latitude and longitude. The meteorological data generated by WRF was coupled with the HYSPLIT Lagrangian code to determine how radioisotopes are expected to spread following the SMR large release.

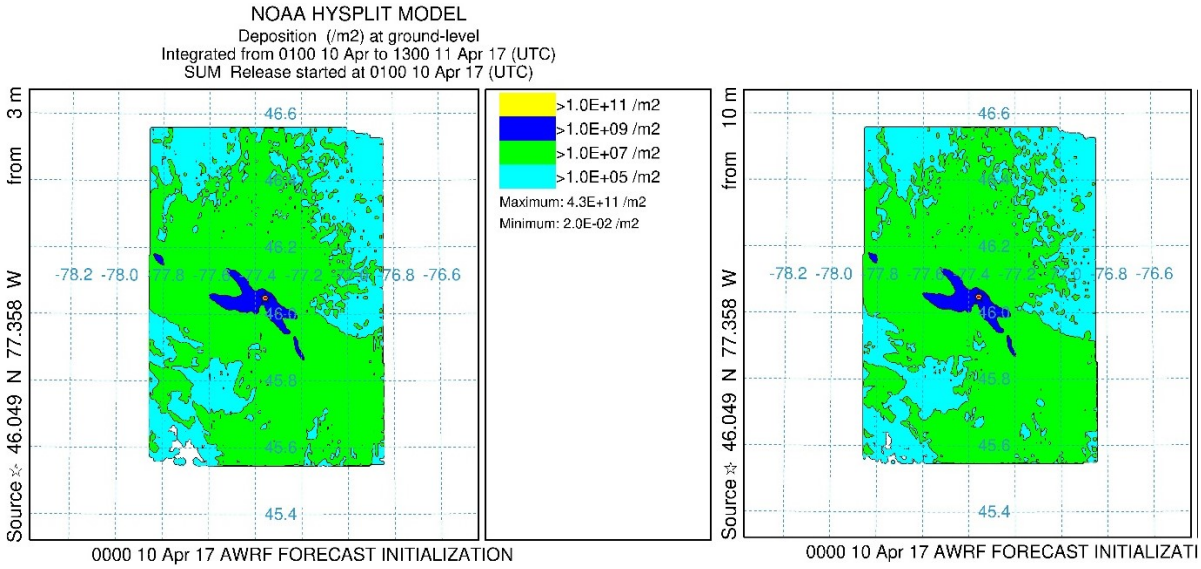

Figure 32 - Comparison of 0 mAGL deposition on 20APR2017; Release point at 3 mAGL (left) and 10 mAGL (right)

The first analysis case, for which the calculated concentration shown in Figure 32, used the following source term

Radionuclide	Amount (Bq)
Iodine-131 particulate	0.591×10^{17}
Iodine-131 gas	1.379×10^{17}
Cesium-137	2.66×10^{15}
Xenon-133	9.20×10^{17}

Table 5 - Source term used with WRF meteorological data

To reiterate, this source term was chosen as a plausible release amount from a SMR following a worst-case accident with no confinement or containment of released gases and particles. Dose rate and total accumulated dose was much higher than that allowed by the Canadian Nuclear Safety Commission over the entire domain.

For reference, a map of the SMR site is given in Figure 33. On the left the political and geographical features of the land near the Ottawa River. The notional SMR location is indicated by the blue star. The geopolitical map has been cropped in order to give a domain approximately equal to the WRF domain. The image on the right shows land use category in a line contour plot. The location of waterbodies near the release point is illustrated.

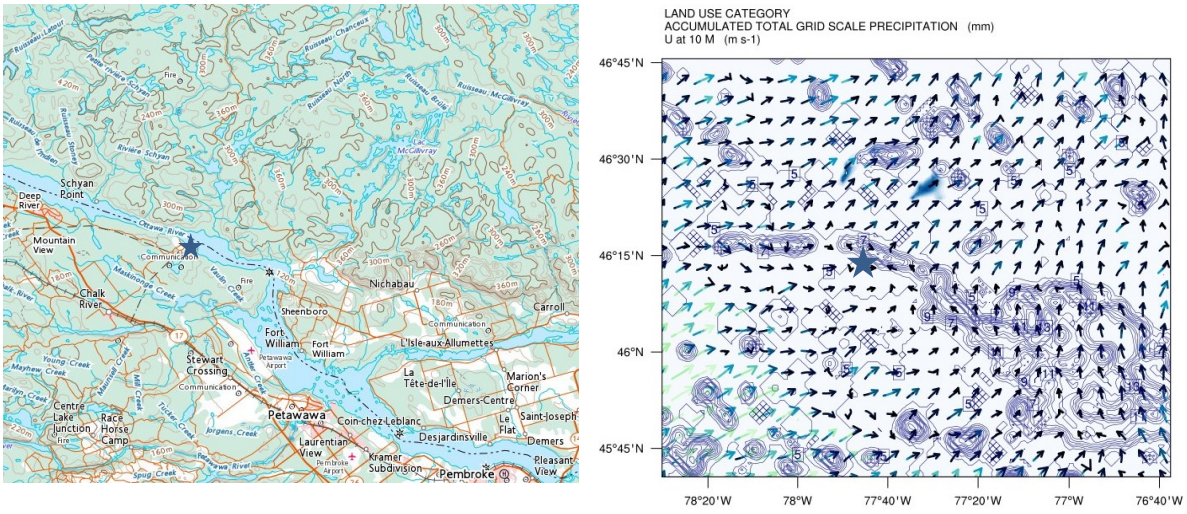

Figure 33 - Geopolitical map showing notional SMR location (left) and land use category contour plot with WRF-calculated wind field on 10APR2017 (right)

It has already been shown that wind fields over the Ottawa River are highly variable with flow sometimes stagnating over the Ottawa River. Vorticity is a notable feature of the wind pattern. It is expected that radionuclides would segregate to the turbulent region with radioactive species becoming caught up in eddies.

Figure 34 consists of a series of radionuclide plots showing concentration up through the atmosphere from ground level to 5000 mAGL for release points at 3 mAGL and 10 AGL. Sub-plots (a) and (b) show radionuclide concentration between 0 and 10 mAGL. When the release occurs at the lower level, 3 mAGL, deposition at this level increases by half to a full order of magnitude. This result is very similar to that of the reanalysis data.

In contrast to the radioactive deposition predicted when using the reanalysis data, the deposition calculated using the WRF data is segregated to the the lowest terrain height – found over the Ottawa River.

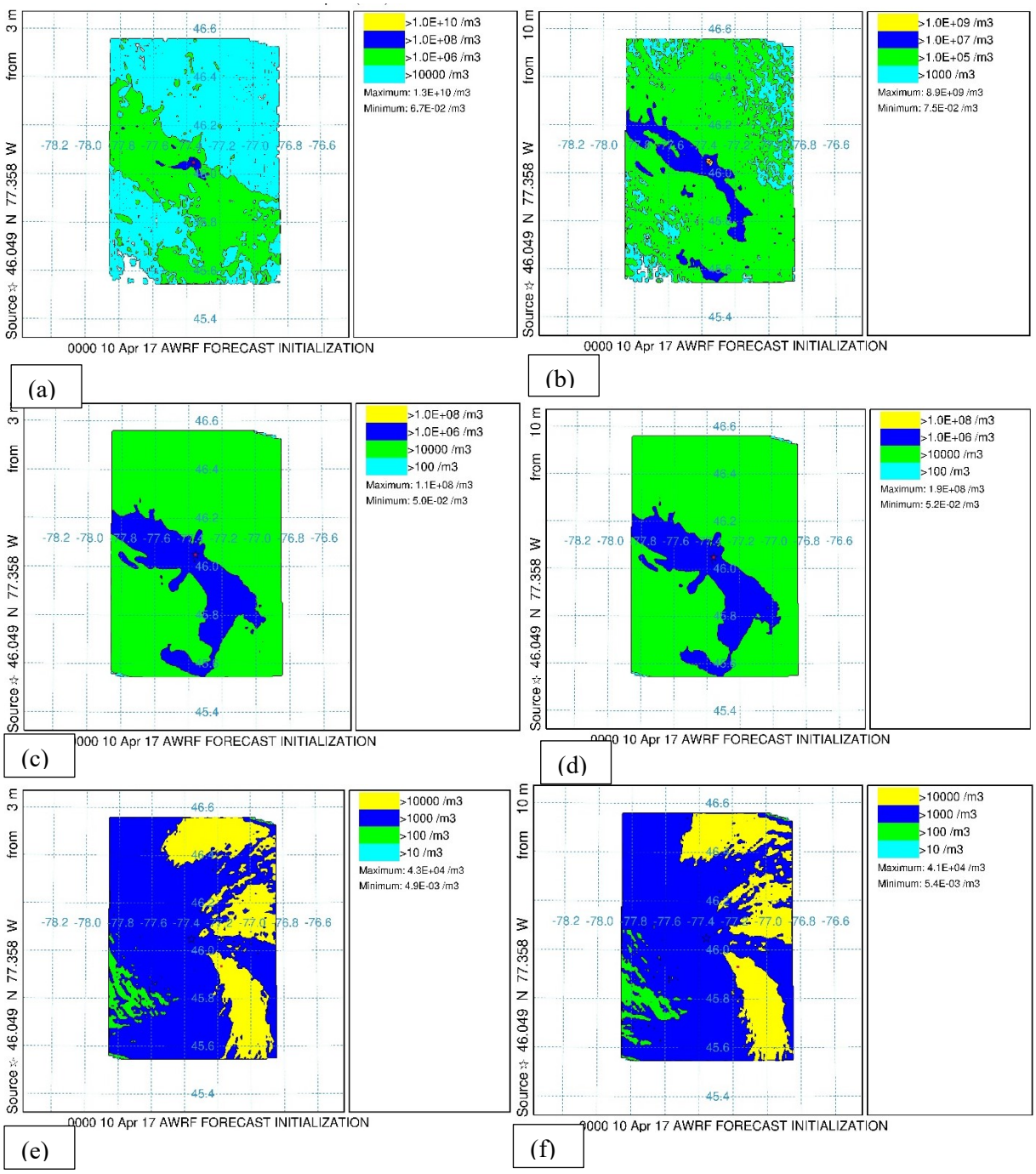

Figure 34 – 20APR2019 0100 hrs UST; Radionuclide concentration between 0-10 mAGL (a, b), 10-500 mAGL (c, d), 500-5000 mAGL (e, f); Release point at 3 mAGL (left) and 10 mAGL (right)

Between 10 and 500 mAGL, plots (c) and (d), the radioisotope concentration is nearly identical regardless of the release point height. The minimum and maximum release concentration is somewhat higher for the higher release point at 10 mAGL. Between 500 and 5000 mAGL, radionuclide dispersion pattern is nearly identical. Minimum and maximum release concentration at this elevation is higher for the lower release point at 3 mAGL. This difference might be attributable to the fact that the top of earth's boundary layer is likely to appear somewhere between 500 and 5000 mAGL.

An interesting thing to note from Figure 34 is that the effect of terrain height appears to diminish between 500 and 5000 mAGL with mean flow dominating over the effect of turbulent eddies. As with the reanalysis data, no radionuclide dispersion was calculated to be present between 5000 and 8000 mAGL.

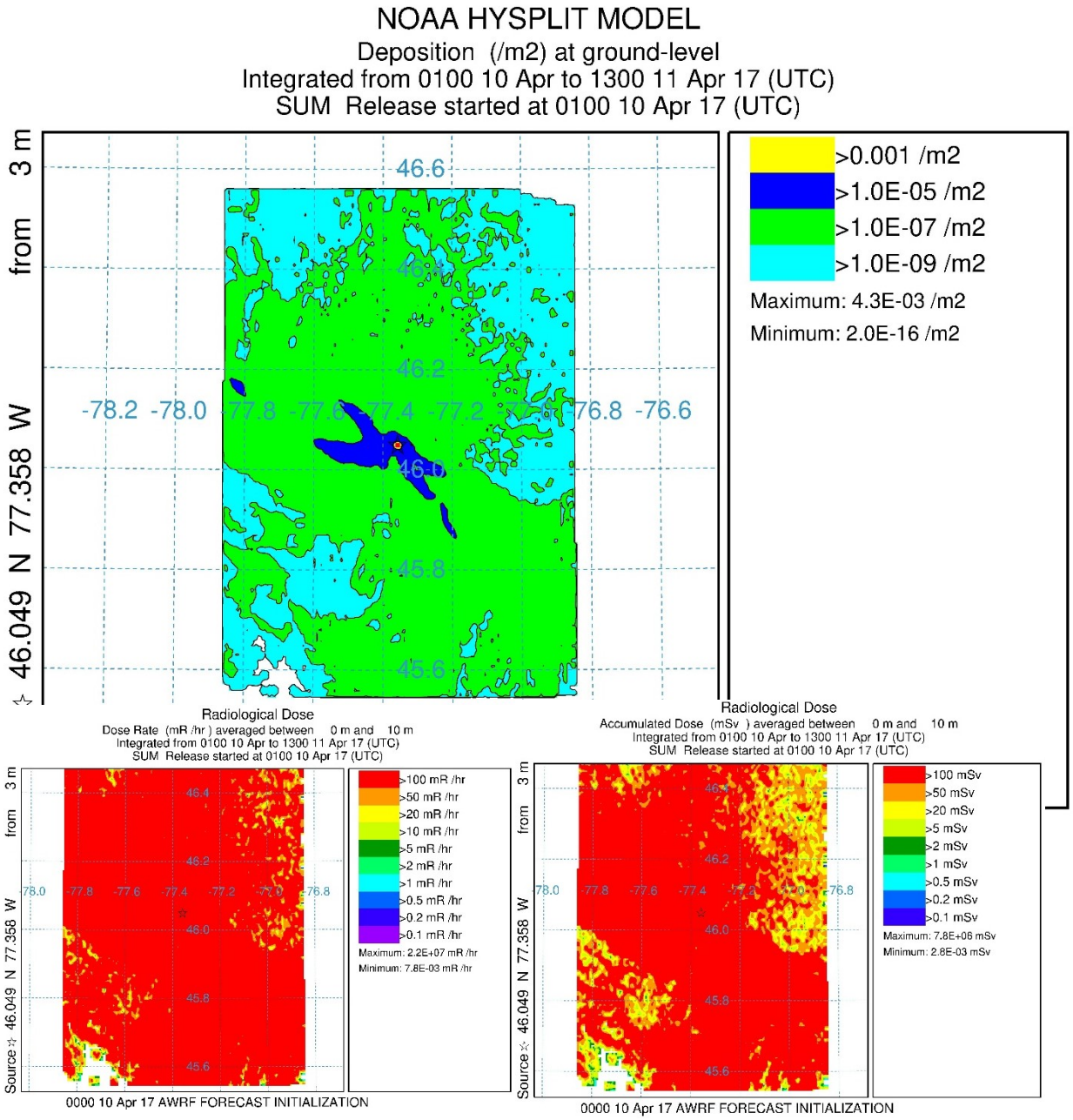

Figure 35 – Deposition at ground level (Bequerels/square meter) Dose rate (mRem/hour) and total dose (milliSieverts) for a release 10^{14} smaller than original source term; 20APR2017

Deposition concentration, dose rate and total dose from Iodine-131, Cesium-137, and Xenon-133 is shown in Figure 35. The source term was 10^{14} Bequerels smaller than the original for each of particulate Iodine-131, gaseous Iodine-131, Cesium-137, and Xenon-133. Maximum total dose was calculated to be 7.8 x 10^{6} milliSieverts higher than the 100 milliSievert limit.

This analysis was completed iteratively with the source term for the second run being reduced by 10^{16} Bequerels for each of the dispersed species. Calculated dose rate and dose on 20APR2017 is lower than for the 10^{14} reduction case with maximum accumulated dose being equal to 7.8 x 10^{4} milliSieverts – still above the public dose threshold.

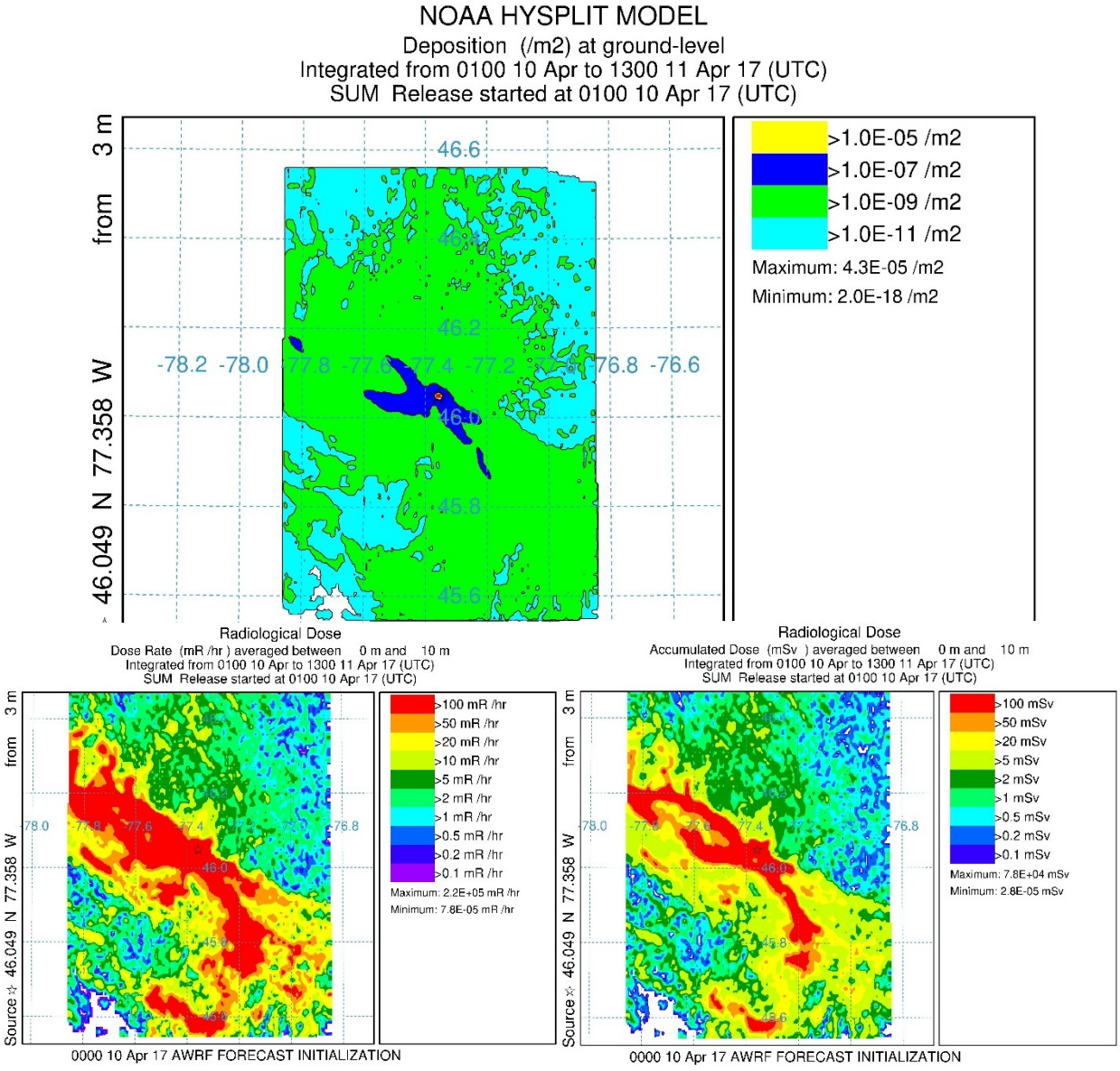

Figure 36 - Dose rate (mRem/hour) and total dose (mSieverts) for a release 10^{16} smaller than original source term; 20APR2017

The third iteration of the analysis used a source term that was reduced by 10^{17} for each of the dispersed species. The results are shown in Figure 37.

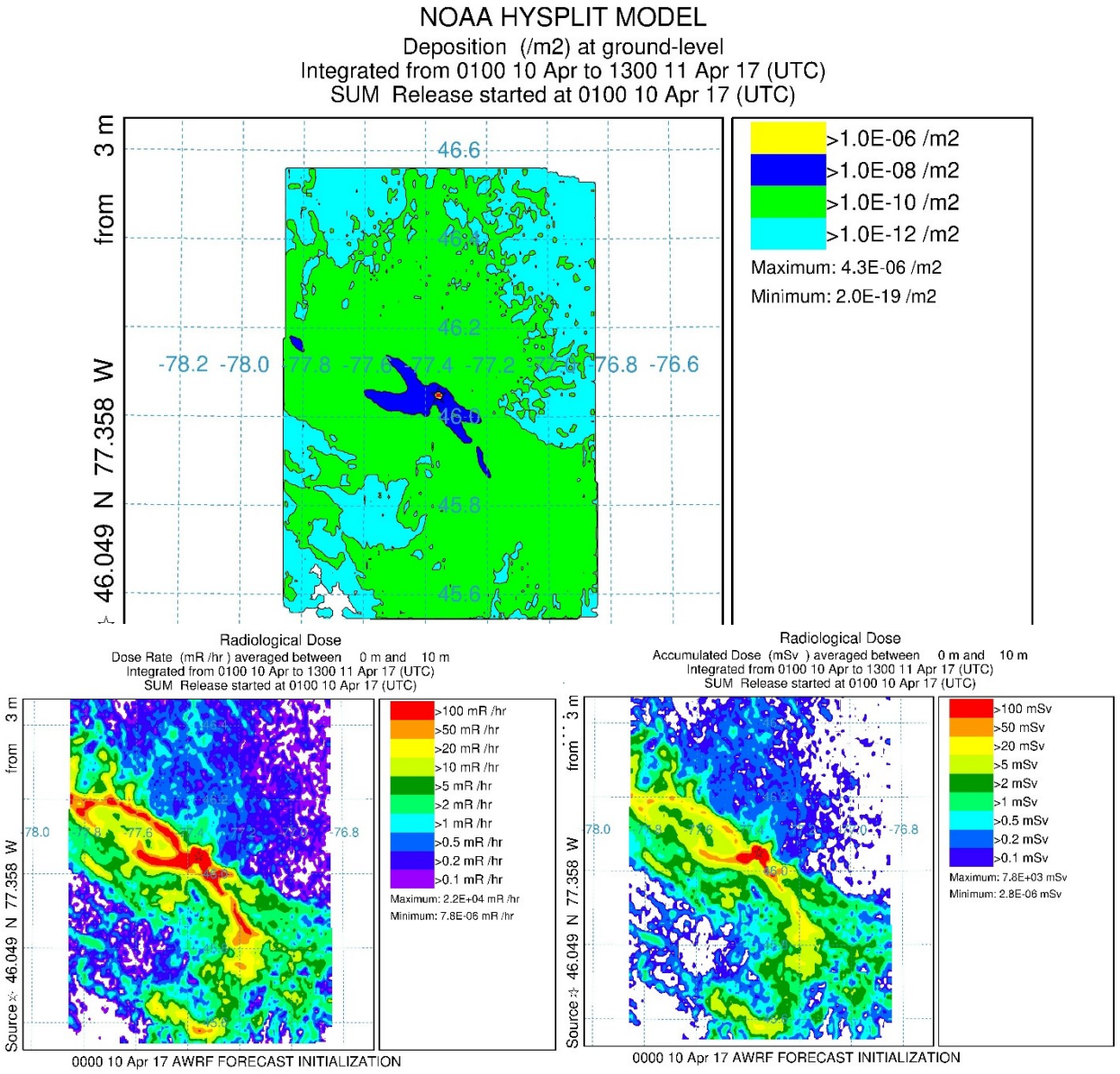

Figure 37 - Dose rate (mRem/hour) and total dose (mSieverts) for a release 10^{17} smaller than original source term; 20APR2017

Calculated dose rate for the third analysis run was reduced and fell in a range between 7.8 x 10^{-6} and 2.2 x 10^{4} millirem per hour. The highest dose rates are concentrated around the

Ottawa River. The accumulated dose is getting closer to the CNSC's limit for acceptable public dose. In the area adjacent to the notional SMR total dose reaches a maximum of 7.8×10^3 milliSieverts.

One futher source term reduction was analyzed. For the final case the source term was 10^{18} times less than the original for each of the species released.

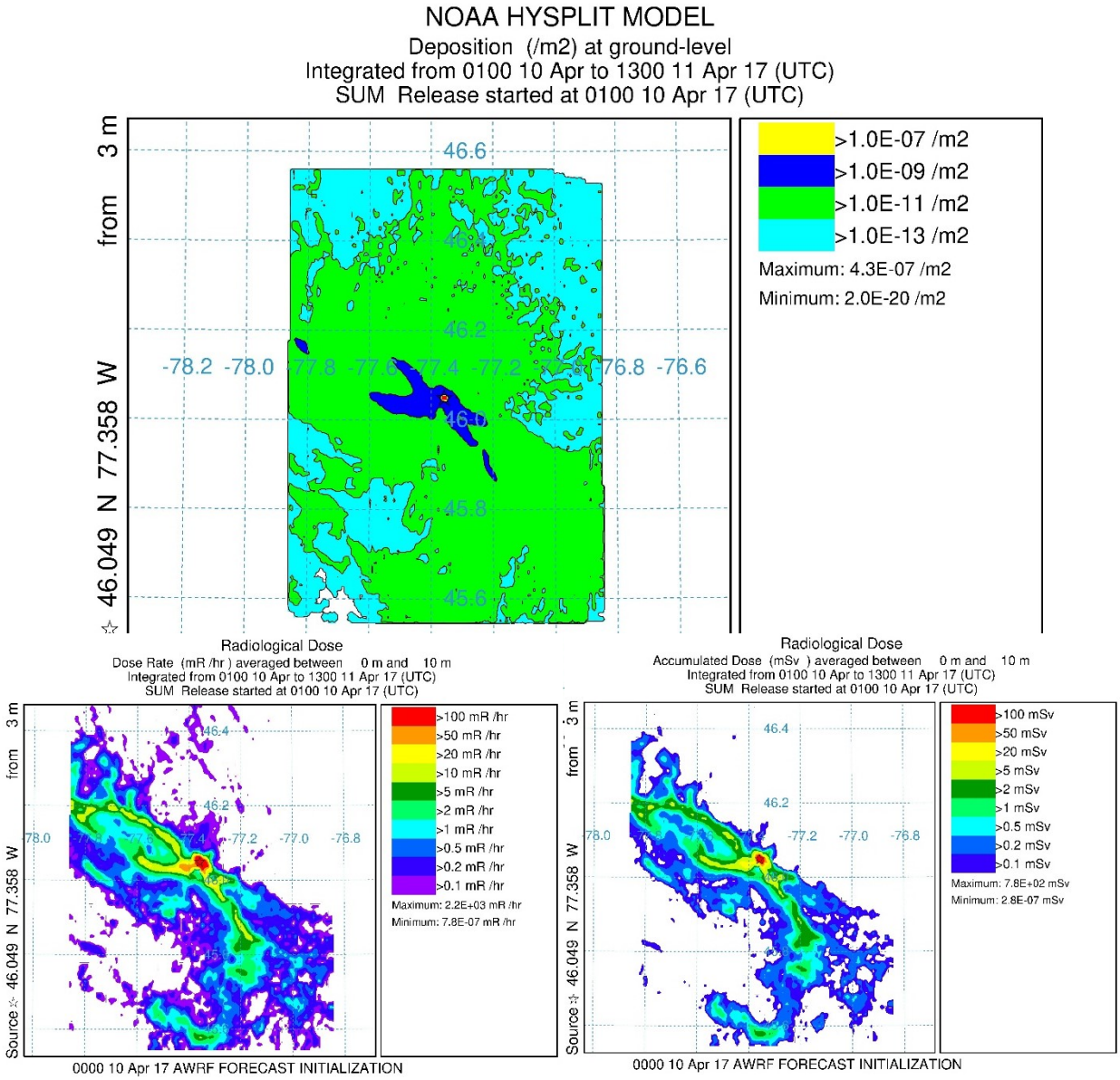

Figure 38 - Dose rate (mRem/hour) and total dose (mSieverts) for a release 10^{18} smaller than original source term; 20APR2017

The results of the final analysis case is shown in Figure 38. As can be seen total accumulated dose reaches a maximum of 780 milliSieverts right at the notional SMR. Communities near the

facility are all located in adjacent areas where total dose range from 2.8 x 10^{-7} to on the order of 20 milliSieverts. No populated areas appear to have dose rates greater than 50 milliSieverts.

5.4 Impact of Simulation Grid Size Used for WRF modelling

Dispersion results generated using HYSPLIT with NARR input data were quite different than those generated using HYSPLIT with WRF-generated data. In order to investigate this further, the WRF simulation was re-run using NARR input data rather than operational data, as was used in the first simulation. The NARR WRF simulation had the same geographical, domain, and physical set up as the operational WRF simulation.

The radionuclide concentration deposition at ground level, in Bequerels per square meter, calculated using the NARR WRF simulation is depicted in Figure 39.

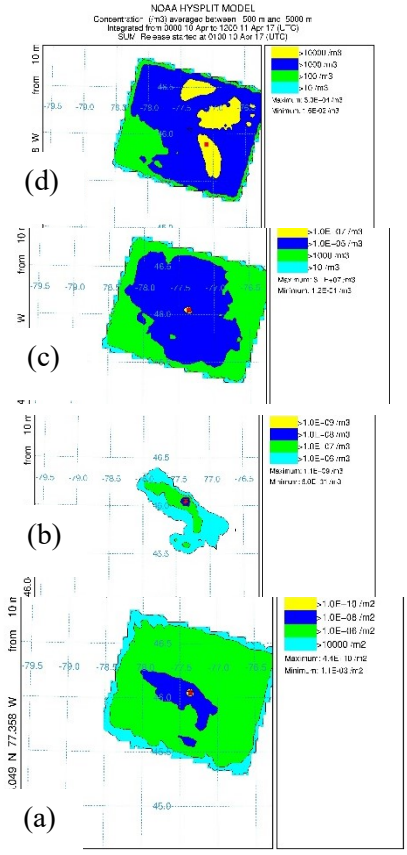

Figure 39 - WRF Simulation Results Using NARR Input Data; (a) radionuclide concentration at ground level, (b) radionuclide concentration averaged 0-10 mAGL, (c) radionuclide concentration averaged 10-500 mAGL, (d) radionuclide concentration averaged 500-5000 mAGL

Comparing Figure 39, showing WRF results using NARR input data, and Figure 34, depicting the WRF simulation using operational data, it can be seen that the shape of the

dispersion is similar. Radionuclide concentrations are higher over the Ottawa River valley in both sets of results.

When the NARR data was used to calculate dispersion directly using HYSPLIT, the dispersion pattern showed a strong directional spread to the north-east of the reactor site. In the simulation having a 148 kilometer by 122 kilometer domain, the same input data yielded a dispersion pattern centered on the reactor site with deposition concentrating in the Ottawa River valley. This dispersion pattern is very similar to the pattern calculated using the NCEP operational input data.

Chapter 6
Conclusion

The data generated in the course of this study certainly supports the need for risk management and mitigation – even for small reactor facilities. A number of the new designs being considered incorporate beneficial features such as passive safety features, water capture of reactor fission products, and completely sealed reactor modules. The safety analysis performed for each design should include calculations that demonstrate such safety features are capable of reducing releases to the environment. Based on the results of this study, the reduction required is around a magnitude of 10^{17} to 10^{18} for a worst-case scenario.

It is prudent to note here that this number is highly sensitive to a number of factors – one being the assumed source term size and composition. Small reactors are still a disruptive force with novel features. As such, the source term for one design may be completely different than for another. One key reason for this is that there are many fuel designs being considered for use in small reactors. This diversity results in the need for each reactor designer to perform a radionuclide dispersion analysis for their particular design to demonstrate that the required radionuclides captured by their design's safety features will be enough to protect workers and the public.

A feature of the Canadian regulatory framework that is particularly favourable for development of small reactors is that operators are responsible for the safety of their facilities. It is up to the operator to demonstrate that the required margin of safety has been attained before a licence to construct will be issued. A second factor that strengthens Canada's position on the global stage is early regulator engagement in designs. This early involvement allows the

independent regulator to provide input and insights into risk and safety management early in the process – possibly before designs are even finalized. This early engagement is highly beneficial to proponents and reactor designers since they are provided with the opportunity to enhance safety while they are still investing in completing their design. This leads to decreased costs and a higher standard of safety performance inherent in the design.

Bibliography

[1] Achim, P., M. Monfort, G. Le Petit, P. Gross, G. Douysset, T. Tafary, X. Blanchard, and C. Moulin. "Analysis of Radionuclide Releases from the Fukushima Dai-ichi Nuclear Power Plant Accident Part II". Pure Appl. Geophys.Vol 171. pp 645 – 667. 2014.

[2] Baklanov, A. and J.H. Sorensen. "Parameterization of Radionuclide Deposition in Atmospheric Long-range Transport Modelling". Physics and Chemistry of the Earth (B). Vol 26. pp 787-799. 2001.

[3] Benamrane, Y., J.-L. Wybo, and P. Armand. "Chernobyl and Fukushima Nuclear Accidents: What Has Changed in the Use of Atmospheric Dispersion Modeling?" Journal of Environmental Radioactivity. Vol 126. pp 239-252. 2013. <http://dx.doi.org/10.1016/j.jenvrad.2013.07.009>.

[4] Bird, R. Byron, Warren E. Stewart, and Edwin N. Lightfoot. *Transport Phenomena*. Revised 2nd Ed. John Wiley & Sons, Inc. 2007.

[5] Black, G., M.A.T. Black, D. Solan, D. Shropshire. "Carbon Free Energy Development and the Role of Small Modular Reactors: A Review and Secision Framework for Deployment in Developing Countries". Renewable and Sustainable Energy Reviews. Vol 43. pp 83-94. 2015.

[6] Blix, H. "The Post-Chernobyl Outlook for Nuclear Power". IAEA Bulletin. pp 9-12. Autumn 1986. <https://www.iaea.org/sites/default/files/28304780912.pdf>. Accessed Jan 19. 2019.

[7] Brandt, J., J.H. Christensen, and L.M. Frohn. "Modelling Transport and Deposition of Caesium and Iodine from the Chernobyl Accident Using the DREAM Model". Atmos. Chem. Phys., Vol 2, pp 397-417. 2002. <https://doi.org/10.5194/acp-2-397-2002>.

[8] Brioude, J., D. Arnold, A. Stohl et al. "Lagrangian Particle Dispersion Model FLEXPART-WRF Version 3.1". Geosci. Model Dev., Vol 6, pp1889-1904. 2013.

[9] Canada. "Radiation Protection Regulations SOR/2000-203". Dec 6. 2018. <https://laws-lois.justice.gc.ca/PDF/SOR-2000-203.pdf>. Accessed 27DEC2018.

[10] Canadian Nuclear Safety Commission. "Introduction to Radiation". Ottawa, Ontario. December 2012. <http://nuclearsafety.gc.ca/eng/pdfs/Reading-Room/radiation/Introduction-to-Radiation-eng.pdf>. Accessed 27FEB2019.

[11] Cantelon, P.L. *A History of the World Association of Nuclear Operators*. Ed. Claire Newell. World Association of Nuclear Operators: London, UK. 2016.

[12] Chino, M., Nakayama, H., Nagai, H., Terada, H., Katata, G., and Yamazawa, H. "Preliminary Estimation of Release Amounts of I-131 and Cs-137 Accidentally Discharged from the Fukushima Daiichi Nuclear Power Plant into the Atmosphere". J. Nucl. Sci. Technol. Vol 48. pp 1129-1134, 2011.

[13] Connan, O., K. Smith, C. Organo, L. Solier, D. Maro, D. Hebert. "Comparison of RIMPUFF, HYSPLIT, ADMS Atmospheric Dispersion Model Outputs, Using Emergency Response Procedures, with 85 KR Measurements Made in the Vicinity of Nuclear Reprocessing Plant". Journal of Environmental Radioactivity. Vol 124. pp 266-277. 2013.

[14] Counihan, J. "Adiabatic Atmospheric Boundary Layers: A Review and Analysis of Data from the Period 1880-1972". Atmospheric Environment. Vol. 9. Pp 871-905. 1975.

[15] Davidson, P.A., *Turbulence an Introduction for Scientists and Engineers.* 2nd Ed. Oxford University Press: New York. 2015.
[16] Deardorff, J.W., "An Explanation of Anomalously Large Reynolds Stresses Within the Convective Planetary Boundary Layer". Journal of the Atmospheric Sciences. Vol 30. September 1973. pp 1070-1076. <https://doi-org.proxy.lib.uwaterloo.ca/10.1175/1520-0469(1973)030%3C1070:AEOALR%3E2.0.CO;2>.
[17] Deardorff, J.W., "Three-dimensional Numerical Modeling of the Planetary Boundary Layer". Workshop on Micrometeorology. D.A. Haugen. Ed. American Meteorological Society. pp 271-311. 1973.
[18] Didier, D., I. Korsakissok, L. Soulhac. *Projet pX: Note de principe pX 1.3*. Institut de Radioprotection et de Sûreté Nucléaire. 2015.
[19] Ding, H., J. Tong, Y. Wang, and L. Zhang. "Development of Emergency Planning Zone for High Temperature Gas-cooled Reactor". Annals of Nuclear Energy. Vol 111. pp 347-353. 2018. <http://dx.doi.org/10.1016/j.anucene.2017.08.039>.
[20] Draxler, R., B. Stunder, G. Rolph, A. Stein, A. Taylor. "HYSPLIT4 User's Guide". Version 4. Revised April. 2018. <https://www.arl.noaa.gov/documents/reports/hysplit_user_guide.pdf>. Accessed 31JAN2019.
[21] Draxler, R.R. and G.D. Hess. *NOAA Technical Memorandum ERL ARL-224: Description of the HYSPLIT_4 Modeling System*. Air Resources Laboratory. December 1997. Revised February 2018.
[22] Eckerman, K.F., and J.C. Ryman. *Exposure-to-dose Coefficients for General Application, Based on the 1987 Federal Radiation Protection Guidance*. Oak Ridge National Laboratory. 1993.
[23] Foudil, Z., B. Mohamed, Z. Tahar. "Estimating of Core Inventory, Source Term and Doses Results for the NUR Research Reactor Under a Hypothetical Severe Accident". Progress in Nuclear Energy. Vol 100. September 2017. pp 365-372. <https://doi.org/10.1016/j.pnucene.2017.07.013>.
[24] Gray, T., M. Whitby, and N. Mann. Periodictable.com. "Cesium-134". 2017. <www.periodictable.com/Isotopes/053.132/index2.dm.html> Accessed 27DEC2018.
[25] Gray, T., M. Whitby, and N. Mann. Periodictable.com. "Iodine-132". 2017. <www.periodictable.com/Isotopes/053.132/index2.dm.html>. Accessed 27DEC2018.
[26] Hu, X., D. Li, H. Huang, S. Shen, and E. Bou-Zeid. "Modeling and Sensitivity Analysis of Transport and Deposition of Radionuclides from the Fukushima Dai-ichi Accident". Atmos. Chem. Phys. Vol 14. pp 11065-11092. 2014.
[27] Huh, C., C. Lin, S. Hsu. "Regional Dispersal of Fukushima-Derived Fission Nuclides by East-Asian Monsoon: A Synthesis and Review". Aerosol and Air Quality Research. Vol 13. pp 537-544. 2013.
[28] International Atomic Energy Agency. "Small modular reactors". 2019. <https://www.iaea.org/topics/small-modular-reactors>. Accessed 4MAR2019.
[29] International Atomic Energy Agency. "Design Safety Considerations for Water Cooled Small Modular Reactor Incorporating Lessons Learned from the Fukushima Daiichi Accident". IAEA TECDOC series 1785. Vienna. 2016. <https://www-pub.iaea.org/MTCD/Publications/PDF/TE-1785_web.pdf>. Accessed 6JAN2019.

[30] International Atomic Energy Agency. “Radiation Protection of the Public and the Environment”. IAEA Safety Standards for Protecting People and the Environment. General Safety Guide No. GSG-8. Vienna. 2018. <https://www-pub.iaea.org/MTCD/Publications/PDF/PUB1781_web.pdf>. Accessed 13JAN2019.
[31] Juniper, M.P. “Chapter 3: Viscous Flow, Fluid Mechanics”. 2015. <http://www2.eng.cam.ac.uk/~mpj1001/learnfluidmechanics.org/LFM_blank_notes/handout_3_v3.pdf>.
[32] Katata, G., M. Ota, H. Terada, M. Chino, H. Nagai. “Atmospheric Discharge and Dispersion of Radionuclides During the Fukushima Dai-ichi Nuclear Power Plant Accident. Part I: Source Term Estimation and Local-scale Atmospheric Dispersion in Early Phase of the Accident”. Journal of Environmental Radioactivity. Vol 109. pp 103-113. 2012.
[33] Korsakissok, I., A. Mathieu, D. Didier. “Atmospheric Dispersion and Ground Deposition Induced by the Fukushima Nuclear Power Plant Accident: A Local-scale Simulation and Sensitivity Study”. Atmospheric Environment. Vol 70. pp 267-279. 2013. <http://dx.doi.org/10.1016/j.atmosenv.2013.01.002>.
[34] Legg, B.J. & M.R. Raupack. “Markov-chain Simulation of Particle Dispersion in Inhomogeneous Flows: The Mean Drift Velocity Induced by a Gradient in Eulerian Velocity Variance”. Boundary-Layer Meteorol Vol 24. Issue 3. 1982. <https://doi-org.proxy.lib.uwaterloo.ca/10.1007/BF00121796>.
[35] Leelossy, A., F. Molnar Jr., F. Izsak, A. Havasi, I. Lagzi, R. Meszaros. “Dispersion Modeling of Air Pollutants in the Atmosphere: A Review” Cent. Eur. J. Geosci. Vol 6 No 3. pp 257-278. 2014. <DOI: 10.2478/s13533-012-0188-6>.
[36] Leelossy, A., R. Meszaros, I. Lagzi. “Short and Long Term Dispersion Patterns of Radionuclides in the Atmosphere Around the Fukushima Nuclear Power Plant”. Journal of Environmental Radioactivity. Vol 102. pp 1117-1121. 2011.
[37] Mahesh, Mahadevappa. “Radiation Dose is X-Ray and CT Exams. Computed Tomography Dose (CT Dose)”. 2018. <https://www.radiologyinfo.org/en/info.cfm?pg=safety-xray>. Accessed 15NOV2018.
[38] Massachusetts Institute of Technology. “2.20 – Marine Hydronamics, Fall 2006. Lecture 2”. <web.mit.edu/13.021/demos/lectures/lecture2.pdf>. Accessed 06MAR2019.
[39] Minister of Public Works and Government Services Canada. “Radon and Health INFO-0813”. Canadian Nuclear Safety Commission. Ottawa. <https://nuclearsafety.gc.ca/pubs_catalogue/uploads/February-2011-Info-0813-Radon-and-Health-INFO-0813_e.pdf>. Accessed 6JAN2019.
[40] Morino, Y., Ohara, T., and Nishizawa, M. “Atmospheric Behavior, Deposition, and Budget of Radioactive Material from the Fukushima Daiichi Nuclear Power Plant in March 2011”. Geophys. Res. Lett. Vol 38, L00G11. 2011. <doi:10.1029/2011g1048689>.
[41] Morino, Y., T. Ohara, M. Watanabe, S. Hayashi, and M. Nishizawa. “Episode Analysis of Deposition of Radiocesium from the Fukushima Daiichi Nuclear Power Plant Accident”. Environmental Science & Technology. Vol 47. pp 2314-2322. 2013. <https://dx.doi.org/10.1021/es304620x>.
[42] National Centers for Environmental Prediction/National Weather Service/NOAA/U.S. Department of Commerce. NCEP FNL Operational Model Global Surface Analyses.

Research Data Archive at the National Center for Atmospheric Research, Computational and Information Systems Laboratory. 1997. <https://doi.org/10.5065/978H-D239>. Accessed 18DEC2018.
[43] National Centers for Environmental Prediction/National Weather Service/NOAA/U.S. Department of Commerce. NCEP FNL Operational Model Global Tropospheric Analyses, continuing from July 1999. Research Data Archive at the National Center for Atmospheric Research, Computational and Information Systems Laboratory, Boulder, CO. 2000. <https://doi.org/10.5065/D6M043C6>. Accessed 19DEC2018.
[44] National Centers for Environmental Prediction/National Weather Service/NOAA/U.S. Department of Commerce. NCEP North American Regional Reanalysis (NARR). Research Data Archive at the National Center for Atmospheric Research, Computational and Information Systems Laboratory. 2005. <http://rda.ucar.edu/datasets/ds608.0/>. Accessed 19DEC2018.
[45] NOAA. "Radioactive Dose and Decay". HYSPLIT Basic Tutorial Contents. N.d. <https://ready.arl.noaa.gov/documents/Tutorial/html/cust_decay.html>. Accessed 18DEC2018.
[46] Nuclear Regulatory Commission. "Backgrounder on the Three Mile Island Accident". NRC Library Document Collections Fact Sheets. 2018. <https://www.nrc.gov/reading-rm/doc-collections/fact-sheets/3mile-isle.html>. Accessed 15MAR2019.
[47] Petti, D.A., R.R. Hobbins, P. Lowry and H. Gougar. "Representative Source Terms and the Influence of Reactor Attributes on Functional Containment in Modular High-Temperature Gas-Cooled Reactors". Nuclear Technology. Vol 184. Iss 2. pp 181-197. 2017. <https://doi.org/10.13182/NT184-181>.
[48] Price, J.F. *Lagrangian and Eulerian Representations of Fluid Flow: Kinematics and the Equations of Motion.* 2006.
[49] Skamarock, W. C., J. B. Klemp, J. Dudhia, D. O. Gill, D. M. Barker, M. G Duda, X.-Y. Huang, W. Wang, and J. G. Powers. "A Description of the Advanced Research WRF Version 3". NCAR Tech. Note NCAR/TN-475+STR. 2008. <doi:10.5065/D68S4MVH>. Accessed 6JAN2019.
[50] Smagorinsky, J., "General Circulation Experiments with the Primitive Equations: 1. The Basic Experiment". Mon. Weather Rev., Vol 91. Number 3. pp 99-164. 1963.
[51] Sportisse, Bruno. "A Review of Parameterizations for Modelling Dry Deposition and Scavenging of Radionuclides". Atmospheric Environment. Volume 41. pp 2683-2698. 2007. <doi:10.1016/j.atmosenv.2006.11.057>.
[52] Srinivas, C.V., R. Venkatesan, R. Baskaran, V. Rajagopal, B. Venkatraman. "Regional Scale Atmospheric Dispersion Simulation of Accidental Releases of Radionuclides from Fukushima Dai-ichi Reactor". Atmospheric Environment. Vol 61. pp 66-84. 2012. <http://dx.doi.org/10.1016/j.atmosenv.2012.06.082>.
[53] Statistics Canada. "Map Projection". Publication 92-195-X. 2018. <https://www150.statcan.gc.ca/n1/pub/92-195-x/2011001/other-autre/mapproj-projcarte/m-c-eng.htm>. Accessed 15MAR2019.
[54] Stein, A.G., R.R. Draxler, G.D. Rolph, B.J.B. Stunder, M.D. Cohen, and F. Ngan. "NOAA's HYSPLIT Atmospheric Transport and Dispersion Modeling System". Bulletin

of the American Meteorological Society. pp 2059-2077. December 2015. <https://journals.ametsoc.org/doi/pdf/10.1175/BAMS-D-14-00110.1>.
[55] Stein, A.F., R.R. Draxler, G.D. Rolph, B.J.B Stunder, M.D. Cohen, and F. Ngan. "Detailed Description of the Model Updates. Supplement to 'NOAA's HYSPLIT Atmospheric Transport and Dispersion Modeling System'". Bulletin of the American Meteorological Society. pp ES-203-ES-207. December 2015. <https://journals.ametsoc.org/doi/suppl/10.1175/BAMS-D-14-00110.1/suppl_file/10.1175_bams-d-14-00110.2.pdf>.
[56] Stohl, A., M. Hittenberger, and G. Wotawa "Validation of the Lagrangian Particle Dispersion Model FLEXPART Against Large Scale Tracer Experiments". Atmos. Environ. Vol 32, 4245-4264. 1998.
[57] Stohl, A., and D. J. Thomson. "A Density Correction for Lagrangian Particle Dispersion Models". Bound.-Layer Met. Vol 90. pp 155-167. 1999.
[58] Stohl, A., C. Forster, A. Frank, P. Seibert, and G. Wotawa. "Technical Note : The Lagrangian Particle Dispersion Model FLEXPART Version 6.2". Atmos. Chem. Phys. Vol 5. pp 2461-2474. 2005.
[59] Stohl, A., P. Seibert, G. Wotawa, D. Arnold, J.F. Burkhard, S. Eckhardt, C. Tapia, A. Vargas, and T.J. Yasunari. "Xenon-133 and Caesium-137 Releases into the Atmosphere from the Fukushima Dai-ichi Nuclear Power Plant: Determination of the Source Term, Atmospheric Dispersion, and Deposition". Atmos. Chem. Phys. Vol 12. pp 2313-2343. 2012.
[60] Srinivas, C.V., R. Venkatesan, R. Baskaran, V. Rajagopal, B. Venkatraman. "Regional Scale Atmospheric Dispersion Simulation of Accidental Releases of Radionuclides from Fukushima Dai-ichi Reactor". Atmospheric Environment. Vol 61. pp 66-84. 2012.
[61] Terada, H., G. Katata, M. Chino, and H. Nagai. "Atmospheric Discharge and Dispersion of Radionuclides During the Fukushima Dai-ichi Nuclear Power Plant Accident. Part II: Verification of the Source Term and Analysis of Regional-Scale Atmospheric Dispersion". Journal of Environmental Radioactivity. Vol 112. pp 141-154. 2012. <doi:10.1016/j.jenvrad.2012.05.023>
[62] "The Atlas of Canada – Toporama". Government of Canada, Her Majesty the Queen in Right of Canada. 2018. <https://atlas.gc.ca/toporama/en/index.html>. Accessed 11JUL2018.
[63] United Nations. "Developments Since the 2013 UNSCEAR Report on the Levels and Effects of Radiation Exposure Due to the Nuclear Accident Following the Great East-Japan Earthquake and Tsunami. A 2015 White Paper to Guide the Scientific Committee's Future Programme of Work". 2015. <http://www.unscear.org/docs/publications/2015/UNSCEAR_WP_2015.pdf>. Accessed 06JAN2019.
[64] United Nations Scientific Committee on the Effects of Atomic Radiation. "The Chernobyl accident". 2012. <www.unscear.org/unscear/en/chernobyl.html>. Accessed 09MAR2019.
[65] United States Nuclear Regulatory Commission. "Backgrounder on the Three Mile Island Accident". 2018. <https://www.nrc.gov/reading-rm/doc-collections/fact-sheets/3mile-isle.html>. Accessed 16MAR2019.

[66] Vié, A., H. Pouransari, R. Zamansky and A. Mani. “Comparison Between Lagrangian and Eulerian Methods from the Simulation of Particle-laden Flows Subject to Radiative Heating”. Center for Turbulence Research Annual Research Briefs. pp 15-27. 2014. <https://web.stanford.edu/group/ctr/ResBriefs/2014/05_vie.pdf>.
[67] Wilson, J.D. and B.L. Sawford. “Review of Lagrangian Stochastic Models for Trajectories in the Turbulent Atmosphere”. Boundary-Layer Meteorology. Vol 78. pp 191-210. 1996.
[68] World Nuclear Association. “Chernobyl Accident 1986”. 2018. <http://www.world-nuclear.org/information-library/safety-and-security/safety-of-plants/chernobyl-accident.aspx>. Accessed 12JUN2018.
[69] World Nuclear Association. “Fukushima Daiichi Accident”. 2018. <http://www.world-nuclear.org/information-library/safety-and-security/safety-of-plants/fukushima-accident.aspx>. Accessed 19JAN2019.
[70] Zeggar, F., B. Mohamed, Z. Tahar. “Estimating of Core Inventory, Source Term and Doses Results for the NUR Research Reactor Under a Hypothetical Severe Accident”. Progress in Nuclear Energy. Vol 100. pp 365-372. 2017. <http://dx.doi.org/10.1016/j.pnucene.2017.07.013>.

Appendix A

Dataset Variables

The variables in the table below are those from the NEP FNL Operational Model Global Tropospheric Analyses. This dataset was used as the input for running the WRF model.

Short Name	Description	Units
TMP	Temperature	K
POT	Potential temperature	K
DPT	Dewpoint temperature	K
APTMP	Apparent temperature	K
SPF H	Specific humidity	kg kg^{-1}
R H	Relative humidity	%
P WAT	Precipitable water	kg m^{-2}
SNO D	Snow depth	m
WEASD	Water equivalent of accumulated snow depth	kg m^{-2}
CLWMR	Cloud water mixing ratio	kg kg^{-1}
CPOFP	Percent frozen precipitation	%
PEVPR	Potential evaporation rate	W m^{-2}
U GRD	u-component of wind	m s^{-1}
V GRD	v-component of wind	m s^{-1}
V VEL	Vertical velocity (pressure)	Pa s^{-1}
ABS V	Absolute vorticity	s^{-1}
GUST	Wind speed (gust)	m s^{-1}
VW SH	Vertical speed shear	s^{-1}
USTM	u-component of storm motion	m s^{-1}
VSTM	v-component of storm motion	m s^{-1}
VRATE	Ventilation rate	m^2 s^{-1}
PRES	Pressure	Pa
PRMSL	Pressure reduced to MSL	Pa
ICAHT	ICAO standard atmosphere reference height	m
HGT	Geopotential height	gpm
GP A	Geopotential height anomaly	gpm
MSLET	MSLP (Eta model reduction)	Pa
5WAVH	5-wave geopotential height	gpm
HPBL	Planetary boundary layer height	m

Short Name	Description	Units
5WAVA	5-wave geopotential height anomaly	gpm
PLPL	Pressure of level from which parcel was lifted	Pa
T CDC	Total cloud cover	%
C WAT	Cloud water	kg m^{-2}
SUNSD	Sunshine duration	s
CAPE	Convective available potential energy	J kg^{-1}
CIN	Convective inhibition	J kg^{-1}
HLCY	Storm relative helicity	m^2 s^{-2}
LFT X	Surface lifted index	deg K
4LFTX	Best (4 layer) lifted index	deg K
TOZNE	Total ozone	Dobson
O3MR	Ozone mixing ratio	kg kg^{-1}
LAND	Land cover (0=sea, 1=land)	Proportion
TSOIL	Soil temperature	K
SOILW	Volumetric soil moisture content	
WILT	Wilting point	
LANDN	Land-sea coverage (nearest neighbor) [land=1, sea=0]	Proportion
FLDCP	Field capacity	
HINDEX	Haines index	
ICEC	Ice cover	fraction

The list of variables below is that from the NARR dataset that was used with the HYSPLIT model.

Short Name	Description	Units
PRES	Pressure	Pa
PRMSL	Pressure reduced to MSL	Pa
HGT	Geopotential height	gpm
TMP	Temperature	K
POT	Potential temp.	K
DPT	Dew point temp.	K
VIS	Visibility	m
UGRD	u wind	$m\ s^{-1}$
VGRD	v wind	$m\ s^{-1}$
VVEL	Vertical velocity (pressure)	$Pa\ s^{-1}$
SPFH	Specific humidity	$kg\ kg^{-1}$
RH	Relative humidity	%
PWAT	Precipitable water	$kg\ m^{-2}$
EVP	Evaporation	$kg\ m^{-2}$
PRATE	Precipitation rate	$kg\ m^{-2}\ s^{-1}$
APCP	Total precipitation	$kg\ m^{-2}$
ACPCP	Convective precipitation	$kg\ m^{-2}$
WEASD	Accum. snow	$kg\ m^{-2}$
SNOD	Snow depth	m
TCDC	Total cloud cover	%
CDCON	Convective cloud cover	%
LCDC	Low level cloud cover	%
MCDC	Mid level cloud cover	%
HCDC	High level cloud cover	%
ALBDO	Albedo	%
TSOIL	Soil temp.	K
SOILM	Soil moisture content	$kg\ m^{-2}$
VEG	Vegetation	%
SNOM	Snow melt	$kg\ m^{-2}$
LHTFL	Latent heat flux	$W\ m^{-2}$
SHTFL	Sensible heat flux	$W\ m^{-2}$
UFLX	Zonal momentum flux	$N\ m^{-2}$
VFLX	Meridional momentum flux	$N\ m^{-2}$
MSLET	Mean sea level pressure (ETA model)	Pa

Short Name	Description	Units
LFTX	Surface lifted index	K
4LFTX	Best (4-layer) lifted index	K
PRESN	Pressure (nearest grid point)	Pa
MCONV	Horizontal moisture divergence	kg kg^{-1} s^{-1}
VWSH	Vertical speed shear	1 s^{-1}
CRAIN	Categorical rain (yes=1; no=0)	
CFRZR	Categorical freezing rain (yes=1; no=0)	
CICEP	Categorical ice pellets (yes=1; no=0)	
CSNOW	Categorical snow (yes=1; no=0)	
SOILW	Volumetric soil moisture (frozen + liquid)	
CLWMR	Cloud water	kg kg^{-1}
GFLUX	Ground Heat Flux	W m^{-2}
CIN	Convective inhibition	J kg^{-1}
CAPE	Convective available potential energy	J kg^{-1}
TKE	Turbulent Kinetic Energy	J kg^{-1}
SOILL	Liquid volumetric soil moisture (non-frozen)	
ICMR	Ice mixing ratio	kg kg^{-1}
CCOND	Canopy conductance	m s^{-1}
HLCY	Storm relative helicity	m^2 s^{-2}
USTM	u-component of storm motion	m s^{-1}
VSTM	v-component of storm motion	m s^{-1}
APCPN	Total precipitation (nearest grid point)	kg m^{-2}
DSWRF	Downward shortwave radiation flux	W m^{-2}
DLWRF	Downward longwave radiation flux	W m^{-2}
MSTAV	Moisture availability	%
SFEXC	Exchange coefficient	(kg m^{-3})(m s^{-1})
USWRF	Upward shortwave radiation flux	W m^{-2}
ULWRF	Upward longwave radiation flux	W m^{-2}
CDLYR	Non-convective cloud	%
HPBL	Planetary boundary layer height	m
CNWAT	Plant canopy surface water	kg m^{-2}
BMIXL	Blackadar's mixing length scale	m
PEVAP	Potential evaporation	kg m^{-2}
SNOHF	Snow phase-change heat flux	W m^{-2}
WVINC	Water vapor added by precip assimilation	kg m^{-2}
WCINC	Water condensate added by precip assimilaition	kg m^{-2}
BGRUN	Subsurface runoff (baseflow)	kg m^{-2}
SSRUN	Surface runoff (non-infiltrating)	kg m^{-2}
WVCONV	Water vapor flux convergence (vertical int)	kg m^{-2}

Short Name	Description	Units
SNOWC	Snow cover	%
WCCONV	Water condensate flux convergence (vertical int)	kg m^{-2}
WVUFLX	Water vapor zonal flux (vertical int)	kg m^{-1}
WVVFLX	Water vapor meridional flux (vertical int)	kg m^{-1}
WCUFLX	Water condensate zonal flux (vertical int)	kg m^{-1}
WCVFLX	Water condensate meridional flux (vertical int)	kg m^{-1}
RCS	Solar parameter in canopy conductance	
RCT	Temperature parameter in canopy conductance	
RCQ	Humidity parameter in canopy conductance	
RCSOL	Soil moisture parameter in canopy conductance	
CD	Surface drag coefficient	
FRICV	Surface friction velocity	m s^{-1}